J. Fluid Mech. (2025), *vol.* 1013, A30, doi:10.1017/jfm.2025.10292

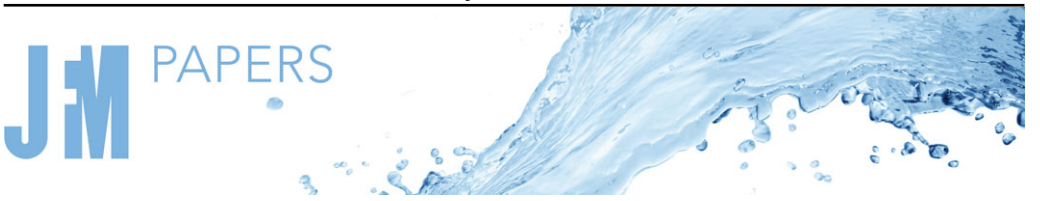

Transversely rotating angular particle in an inertial flow at moderate Reynolds numbers

Guodong Gai[1] **and Anthony Wachs**[1,2]

[1]Department of Mathematics, University of British Columbia, Vancouver, BC, Canada

[2]Department of Chemical & Biological Engineering, University of British Columbia, Vancouver, BC, Canada

Corresponding author: Anthony Wachs, wachs@math.ubc.ca

(Received 21 November 2024; revised 26 March 2025; accepted 22 May 2025)

We investigate the dynamics, wake instabilities and regime transitions of inertial flow past a transversely rotating angular particle. We first study the transversely rotating cube with a four-fold rotational symmetry axis (RCF4), elucidating the mechanisms of vortex generation and the merging process on the cube surface during rotation. Our results identify novel vortex shedding structures and reveal that the rotation-enhanced merging of streamwise vortex pairs is the key mechanism driving vortex suppression. The flow inertia and particle rotation are demonstrated to be competing factors that influence wake instability. We further analyse the hydrodynamic forces on the rotating cube, with a focus on the Magnus effect, highlighting the influence of sharp edges on key parameters such as lift, drag, rotation coefficients and the shedding frequency. We note that the lift coefficient is independent of flow inertia at a specific rotation rate. We then examine more general angular particles with different numbers of rotational symmetry folds – RTF3 (three-fold tetrahedron), RCF3 (three-fold cube) and ROF4 (four-fold octahedron) – to explore how particle angularity and rotational symmetry affect wake stability, regime transitions and hydrodynamic forces. We show that the mechanisms of vortex generation and suppression observed in RCF4 apply effectively to other angular particles, with the number of rotational symmetry folds playing a crucial role in driving regime transitions. An increased rotational symmetry fold enhances vortex merging and suppression. Particle angularity has a pronounced influence on hydrodynamic forces, with increased angularity intensifying the Magnus effect. Furthermore, the number of effective faces is demonstrated to have a decisive impact on the shedding frequency of the wake structures. Based on the number of effective faces during rotation, we propose a generic model to predict the Strouhal number, applicable to all the angular particles studied. Our results demonstrate that the particle angularity and rotational symmetry can be effectively harnessed to stabilise the wake flow. These findings provide novel insights into the complex interactions

© The Author(s), 2025. Published by Cambridge University Press. This is an Open Access article, distributed under the terms of the Creative Commons Attribution licence (https://creativecommons.org/licenses/by/4.0/), which permits unrestricted re-use, distribution and reproduction, provided the original article is properly cited.

https://doi.org/10.1017/jfm.2025.10292 Published online by Cambridge University Press

between particle geometry, rotation and flow instability, advancing the understanding of the role sharp edges play in inertial flow past rotating angular particles.

Key words: particle/fluid flow, vortex shedding, vortex streets

1. Introduction

Particle-laden multiphase flows have long been, and actively remain, a critical area of study due to their broad application in various natural and industrial processes. These flows are essential for understanding applications such as sediment transport in rivers (Mercier *et al.* 2020; Seyed-Ahmadi & Wachs 2021), polluant dispersion in oceans (Rahmani *et al.* 2022, 2023), fluidised beds in chemical engineering (Dupuy, Ansart & Simonin 2024; Hardy, Fede & Simonin 2024) and bubbly flows in mechanical engineering (Chaparian & Frigaard 2021; Bonnefis *et al.* 2024). The study of flows around rotating bluff bodies, including spheres, cylinders and other non-spherical particles, is essential for understanding the dynamics of these multiphase flows. It is well-established that the flow past a fixed bluff body, beyond a critical Reynolds number, leads to asymmetrical vortex shedding behind the body. These vortex-induced fluctuations are a primary cause of flow-induced vibration and fatigue, which, in extreme cases, may result in structural failure. Assigning rotation to the bluff body significantly modifies the flow dynamics compared with fixed bodies, potentially eliminating or reducing vortex shedding and the associated oscillations (Rashidi, Hayatdavoodi & Esfahani 2016). These insights are critical for addressing various natural and engineering challenges, such as optimising the performance of drilling pipes (Chen *et al.* 2020). Furthermore, the rotational dynamics of freely settling particles play a key role in determining path instability of individual particles (Gai & Wachs 2024), while also influencing the microstructure and collective behaviour of particle suspensions in inertial flow (Seyed-Ahmadi & Wachs 2019; Goyal *et al.* 2024) and turbulent boundary layers (Baker & Coletti 2021). Although extensive research has been conducted on flow past spheres and cylinders, flow interactions with rotating angular particles are less understood. Unlike their streamlined counterparts, angular particles with sharp edges and corners exhibit distinct flow characteristics, particularly in vortex generation and wake instability. This study seeks to address this gap by providing deeper insights into the complex flow interactions with a transversely rotating angular isometric polyhedron, uncovering the unique dynamics and behaviours that emerge from these interactions. In the following, we review the current understanding of flow past transversely rotating objects, such as spheres and cylinders, to provide context and clarify our motivation for focusing on the more complex and intriguing behaviour of rotating angular particles.

The dynamics of a flow around a rotating sphere has long attracted research interest and has been extensively studied, largely due to the simple geometry of the sphere. In both natural and industrial applications, transverse rotation is far more common than streamwise rotation in most practical scenarios, making it a key focus in the literature (Torobin & Gauvin 1959). A uniform flow past a transversely rotating sphere gives rise to a transverse hydrodynamic force known as the Magnus effect, which causes a deflection in the flight path of a freely moving sphere. Rubinow & Keller (1961) were among the first to investigate these dynamics in Stokes flow, discovering that while the drag force remains independent of rotation and equal to the Stokes drag, the lift coefficient is proportional to the rotation rate, expressed as $C_l = 2\Omega$, where Ω is the dimensionless rotation rate of the particle, using the free stream velocity and the sphere radius as reference scales.

https://doi.org/10.1017/jfm.2025.10292 Published online by Cambridge University Press

For inertial flow, Tsuji, Morikawa & Mizuno (1985) assumed a proportional relationship between lift and rotation, and proposed the correlation $C_l = (0.4 \pm 0.1)\Omega$ for Reynolds numbers $550 \leqslant Re \leqslant 1600$ and rotation rates $\Omega < 0.7$. Oesterlé & Dinh (1998) focused on lower Reynolds numbers, $10 \leqslant Re \leqslant 140$, and higher rotation rates, $1 \leqslant \Omega \leqslant 6$, providing a correlation based on experimental data: $C_l = 0.45 + (2\Omega - 0.45)\exp(-0.075\Omega^{0.4}Re^{0.7})$. For moderate flow inertia ($100 \leqslant Re \leqslant 500$) and low rotation rates ($0.16 \leqslant \Omega \leqslant 0.5$), Niazmand & Renksizbulut (2003) introduced another empirical correlation: $C_l = 0.11(1 + \Omega)^{3.6}$. Unless otherwise specified, Re is computed using the free stream velocity and the sphere diameter for a meaningful comparison with published work. Further efforts have been made to generalise these empirical correlations over broader ranges of Re and Ω, with these advancements thoroughly summarised by Shi & Rzehak (2019). In general, the lift coefficient C_l of a rotating sphere increases with Ω, but decreases with Re. A bifurcation effect occurs around $Re = 200$, which significantly influences the Magnus effect, particularly at low rotation rates (Shi & Rzehak 2019).

With regards to wake instability, the flow at low inertia past a rotating sphere undergoes a series of regime transitions, characterised by changes in wake vortical structures, as Re and Ω vary. For low Re at $\Omega < 0.5$, the rotation can trigger a vortex shedding, with the shedding frequency Str modulated by Ω (Best 1998; Niazmand & Renksizbulut 2003). As the rotation rate increases, the mean length of the recirculation region progressively shrinks and shifts towards the high-pressure side, eventually disappearing entirely for $\Omega > 0.5$. The fluid passing through the low-pressure region is dragged along the lee side of the sphere until it encounters fluid moving downstream over the high-pressure side, where it is peeled off the sphere surface to form a shear layer. At $Re = 250$, vortex suppression occurs around $\Omega = 0.3$, where two steady vortical threads form in the wake region, and the flow remains steady (Giacobello, Ooi & Balachandar 2009). At a higher Reynolds number of $Re = 300$, periodic vortex shedding reappears for $\Omega \geqslant 0.8$, where the vortical threads in the near-wake tilt and evolve into a one-sided hairpin structure, driven by oblique Kelvin–Helmholtz instability (Giacobello *et al.* 2009; Poon *et al.* 2013). With further increase of the flow inertia beyond $Re \geqslant 500$ and $\Omega \geqslant 0.8$, the flow structures transition into the shear layer stable foci regime before becoming fully chaotic (Poon *et al.* 2014). A second type of studies investigates the turbulent regimes, $Re \geqslant 10^4$, particularly focusing on the inverse Magnus effect (Kim *et al.* 2014). Recent experiments have revealed varying Magnus effects, in the intermediate range of $10^3 \leqslant Re \leqslant 10^4$ (Sareen, Hourigan & Thompson 2024). At extremely high rotation rates, $\Omega \geqslant 4$, upstream vortex shedding has been observed, characterised by the formation of multiple small-scale vortex filaments (De & Sarkar 2023). Additionally, many studies have explored wake instability in the flow past a rotating sphere through linear and weakly nonlinear analyses, shedding light on the competitive interactions of global modes in pattern formation (Citro *et al.* 2016; Jiménez-González *et al.* 2019; Sierra-Ausín *et al.* 2022). These analyses provide deep insights into the mechanisms driving flow transitions and vortex dynamics in various regimes of transversely rotating spheres.

In addition to spheres, bluff bodies with non-spherical geometries, particularly cylinder-like shapes, have also been the focus of extensive research. In two-dimensional (2-D) simulations, vortex suppression has been observed in rotating circular and square cylinders (Kang, Choi & Lee 1999; Khan *et al.* 2021; Karimi-Zindashti & Kurç 2024). A distinctive feature of flow past rotating square cylinders is the development of near-field wakes along the upper or lower (depending on the rotation direction) side of the square, which evolve independently from the main wake and differ significantly from the case of circular cylinders or spheres (Karimi-Zindashti & Kurç 2024). Yang *et al.* (2023) explored three-dimensional flow dynamics around a rotating circular cylinder of finite length with

https://doi.org/10.1017/jfm.2025.10292 Published online by Cambridge University Press

the axis perpendicular to the flow at $Re < 500$ and $\Omega \leqslant 2$. For a cylinder with aspect ratio of 1 and $\Omega \leqslant 0.3$, the wake pattern is similar to that of a fixed cylinder, though with a new linearly unstable mode competing to dominate the wake saturation state. At $\Omega \geqslant 0.9$, a new low-frequency wake structure emerges, characterised by stronger oscillations. Yang *et al.* (2023) also identified new flow modes and conducted global stability analyses, finding that the dynamics of a rotating short cylinder with an aspect ratio slightly greater than 1 resembles that of a rotating sphere. As the aspect ratio increases, the flow becomes increasingly unstable at $\Omega < 0.6$, emphasising the significant influence of particle shape on wake instability.

In recent years, there has been a growing interest in the flow interactions with angular particles, driven by their unique behaviours in fluid flow and critical roles in chemical and mechanical engineering processes (Seyed-Ahmadi & Wachs 2019; Angle, Rau & Byron 2024; Marquardt, Hafen & Krause 2024; Wang *et al.* 2024). A exemplary case is the use of soft hydro-gel cubes, which swell in response to changes in pressure, temperature and pH of the flow environment. These hydrogel cubes present an innovative approach for detecting fluctuations in brain fluids, offering significant potential for non-invasive *in vivo* diagnostics (Tang *et al.* 2024). As a result, understanding the intricate flow interactions with angular particles, such as cubes, is becoming increasingly vital for advancing technological applications. Numerous studies have examined the interactions between flows and fixed angular particles. Saha (2004) conducted body-fitted numerical simulations of the laminar flow past a fixed cube at $20 \leqslant Re_{edge} \leqslant 300$, with Re_{edge} the Reynolds number based on cube edge length. They found that the transition sequence and flow structures are comparable to those observed around a fixed sphere, although with different critical Reynolds numbers of regime transition. Later, Klotz *et al.* (2014) carried out an extensive experimental investigation of the wake behind a fixed cube for $20 \leqslant Re_{edge} \leqslant 400$, using particle image velocimetry and laser-induced fluorescence. Their study identified two bifurcations indicating the transition from steady to unsteady flow regimes. More recently, Meng *et al.* (2021) performed high-fidelity body-fitted numerical simulation of flows past a fixed cube at $1 \leqslant Re_{edge} \leqslant 400$, providing accurate critical Reynolds numbers for regime transition further confirmed by weakly nonlinear instability analysis. In our previous works, we systematically explored the flow behaviour past a fixed Platonic polyhedron at $100 \leqslant Re \leqslant 500$ (Gai & Wachs 2023*a*,*c*,*d*). Our findings revealed that both the angularity and the angular position of the particle significantly influence wake structures in steady and unsteady regimes. In the steady regime, the generation of streamwise vortex pairs is determined by the inclined particle front faces. The shape of the particle significantly influences the recirculation region, resulting in distinct vortex shedding patterns. These dynamic wake features, in turn, modify the hydrodynamic force and torque acting on the particle (Gai & Wachs 2023*b*). In terms of moving angular particles, new regimes, such as the helical settling regime, emerge for freely settling Platonic polyhedrons in quiescent flow, driven by enhanced rotation of particles with high angularity (Rahmani & Wachs 2014; Seyed-Ahmadi & Wachs 2019; Gai & Wachs 2024). Daghooghi & Borazjani (2018) demonstrated that irregular-shaped particles, which have more extended surface areas or mass distributions farther from their centres, experience amplified hydrodynamic forces. They further showed that modelling such particles using simple regular shapes can lead to underestimation of both stress and viscosity, emphasising the critical role of realistic particle shape in accurately predicting suspension rheology.

Despite these valuable insights gained for fixed and freely moving angular particles, our understanding of the flow dynamics around rotating angular particles remains limited. To bridge this gap, we investigate the flow past a transversely rotating cube at moderate Reynolds numbers and extend the analysis to other isometric angular polyhedrons,

https://doi.org/10.1017/jfm.2025.10292 Published online by Cambridge University Press

including the tetrahedron and octahedron, to gain a more comprehensive understanding. This study aims to address four key questions: (i) what drives vortex generation on the surface of a rotating angular particle?; (ii) what mechanisms control the suppression and reemergence of vortex shedding behind angular particles?; (iii) how do rotational symmetry and particle geometry affect wake stability and regime transitions?; and (iv) what impact does particle angularity have on hydrodynamic forces?

The rest of the paper is organised as follows. Section 2 outlines the numerical methods, defines the dimensionless parameters and details the simulation set-up. Section 3 presents the numerical validation of the flow past a rotating sphere. In § 4, we provide a detailed analysis of the flow dynamics around a rotating cube, with a focus on regime transitions, on vortex generation and merging, and on the influence of rotation on wake instability, hydrodynamic forces and vortex shedding frequency. Building on the insights gained from the rotating cube, § 5 expands the investigation to other angular particles, specifically tetrahedrons and octahedrons, with different numbers of rotational symmetry folds. Finally, § 6 presents the key conclusions and potential perspectives for future research.

2. Numerical method, dimensionless numbers and numerical set-up

The distributed Lagrange multiplier/fictitious domain (DLM/FD) method simulates a rigid body immersed in the fluid by introducing a fictitious domain P. Within this domain, rigid-body constraints are enforced to ensure it behaves like a rigid particle. Throughout this paper, dimensional quantities are indicated with a superscript *, while non-dimensional quantities are presented without any superscript. We consider a large cubic computational domain $\mathcal{D}$ with boundary Γ, containing a solid sub-domain P, which represents a rigid body immersed in a Newtonian fluid with constant density ρ_f^* and viscosity μ_f^*. To clearly distinguish between the fluid and solid regions, the fluid sub-domain is defined as $\mathcal{D} \setminus P$, ensuring no overlap between the fluid and solid domains, i.e. $\mathcal{D} \setminus P \cap P = \emptyset$. The DLM/FD method used in this study has been thoroughly discussed and validated in prior works (Glowinski *et al.* 1999; Wachs 2009, 2011; Wachs *et al.* 2015; Selçuk *et al.* 2021). For the sake of brevity, we present only a brief overview of the governing equations for fluid motion and the coupled equations governing the motion of the particle–fluid mixture in Appendix A.

2.1. *Dimensionless numbers*

The governing equations (A1)–(A2) can be non-dimensionalised using the following reference scales: the reference length $L_{ref}^* = D_{sph}^*$, where D_{sph}^* is the diameter of the volume-equivalent sphere defined later; the reference velocity $U_{ref}^* = U_0^*$, corresponding to the incoming flow velocity; the reference time scale L_{ref}^*/U_{ref}^*; the reference pressure $\rho_f^* U_{ref}^{*,2}$ and the reference moment of inertia tensor $\rho_s^* L_{ref}^{*,5}$.

The key dimensionless quantities considered in this study are: (i) the particle Reynolds number Re, the rotational rate Ω, the particle angularity ϕ and rotational symmetry fold n_Ω; and (ii) output parameters such as the lift coefficient C_l, the drag coefficient C_d, the rotation coefficient C_Ω, the vortex shedding frequency $\mathcal{S}tr$ and the dimensionless vorticity $\boldsymbol{\omega}$, along with other relevant quantities.

The particle Reynolds number Re is defined as

$$Re = \frac{\rho_f^* U_{ref}^* D_{sph}^*}{\mu_f^*}. \tag{2.1}$$

https://doi.org/10.1017/jfm.2025.10292 Published online by Cambridge University Press

Since we consider different angular particles with the same volume, Re is defined based on the diameter of a sphere with the same volume as the angular particle, referred to as the volume-equivalent sphere and computed by

$$D^*_{sph} = \left(\frac{6}{\pi} V^*_{Particle}\right)^{1/3}, \tag{2.2}$$

where $V^*_{Particle}$ is the volume of the angular particle.

Particle sphericity, denoted by ϕ, quantifies how closely an angular particle resembles a perfect sphere. Specifically, ϕ is defined as the ratio of the surface area of the volume-equivalent sphere, S^*_{sph}, to the surface area of an angular particle, S^*_p, as given by the following equation:

$$\phi = \frac{S^*_{sph}}{S^*_p}. \tag{2.3}$$

The level of non-sphericity is inversely proportional to ϕ. When ϕ is close to 1, the particle shape closely approximates a sphere. In the present study, non-sphericity is equivalent to angularity, and the level of angularity is inversely proportional to ϕ. As expected, we have $\phi_{tetrahedron} < \phi_{cube} < \phi_{octahedron}$.

We define the dimensionless rotation rate as follows:

$$\boldsymbol{\Omega} = \frac{\boldsymbol{\Omega^*} D^*_{sph}}{2U^*_{ref}}, \tag{2.4}$$

where $\boldsymbol{\Omega^*}$ represents the rotation rate of the angular particle around the transverse direction, chosen here as the z direction. During the rotation, the number of rotational symmetry folds n_Ω refers to the number of times an angular particle can be rotated by equal angles around the rotation axis and still appear identical to its original angular position.

The drag coefficient C_d and the lift coefficients $C_{l,y}$ and $C_{l,z}$ for a rotating particle are defined as follows:

$$C_d = \frac{8F^*_x}{\pi\rho^*_f {U^*_{ref}}^2 D^{*,2}_{sph}}, \quad C_{l,y} = \frac{8F^*_y}{\pi\rho^*_f {U^*_{ref}}^2 D^{*,2}_{sph}}, \quad C_{l,z} = \frac{8F^*_z}{\pi\rho^*_f {U^*_{ref}}^2 D^{*,2}_{sph}}, \tag{2.5}$$

where $\boldsymbol{F}^*$ denotes the hydrodynamic force exerted on the angular particle. Similarly, the torque coefficients are calculated as

$$T_x = \frac{8T^*_x}{\pi\rho^*_f U^{*,2}_{ref} D^{*,3}_{sph}}, \quad T_y = \frac{8T^*_y}{\pi\rho^*_f U^{*,2}_{ref} D^{*,3}_{sph}}, \quad T_z = \frac{8T^*_z}{\pi\rho^*_f U^{*,2}_{ref} D^{*,3}_{sph}}, \tag{2.6}$$

where T^*_i represents the ith component of the hydrodynamic torque $\boldsymbol{T^*}$ for $i \in \{x, y, z\}$. Please note that in the context of the DLM/FD method (Seyed-Ahmadi & Wachs 2020), the hydrodynamic force $\boldsymbol{F}^*$ and torque $\boldsymbol{T}^*$ are calculated using the integral of the Lagrange multipliers over P, such that

$$\boldsymbol{F}^* = \int_P \boldsymbol{\lambda}^* \mathrm{d}\boldsymbol{x}, \quad \boldsymbol{T^*} = \int_P \boldsymbol{r} \times \boldsymbol{\lambda}^* \mathrm{d}\boldsymbol{x}. \tag{2.7}$$

Furthermore, the rotation coefficient C_Ω is introduced to quantify the relationship between the Magnus lift force and the rotation rate $\Omega^* = ||\boldsymbol{\Omega^*}||$. It is calculated as

$$C_\Omega = \frac{6F^*_y}{\pi\rho_f U^*_{ref} D^{*,3}_{sph} \Omega^*}. \tag{2.8}$$

https://doi.org/10.1017/jfm.2025.10292 Published online by Cambridge University Press

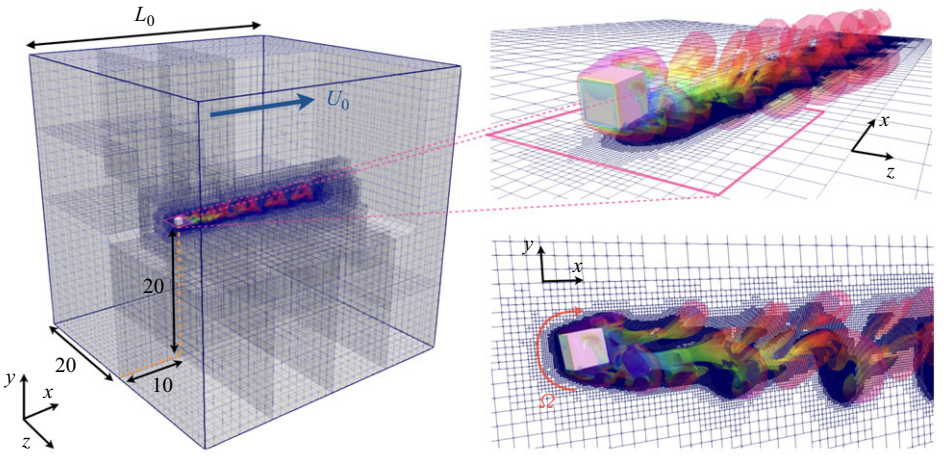

Figure 1. Computational domain and wake structures of the flow past a rotating cube at $\Omega = 0.3$ and $Re = 200$ with a four-fold rotational symmetry axis (RCF4) aligned along the z-axis. Vortical structures, identified by $\lambda_2 = -1$, are coloured by the streamwise velocity u_x (red indicating high velocity, blue indicating low velocity). The right panels show adaptive mesh refinement on both the x-z and x-y cut planes.

The Strouhal number characterises the oscillatory behaviour of the flow in the wake of the particle and is defined as

$$\mathcal{S}tr = \frac{f_c^* D_{sph}^*}{U_{ref}^*}, \tag{2.9}$$

By normalising f_c^* with U_{ref}^*/D_{sph}^*, which corresponds to the inverse of the advective time scale, the $\mathcal{S}tr$ captures the characteristic frequency of vortex shedding.

To better visualise the wake structures, the dimensionless vorticity, which measures fluid rotation, is computed as follows:

$$\omega_x = \frac{\omega_x^* D_{sph}^*}{U_{ref}^*}, \quad \omega_y = \frac{\omega_y^* D_{sph}^*}{U_{ref}^*}, \quad \omega_z = \frac{\omega_z^* D_{sph}^*}{U_{ref}^*}, \tag{2.10}$$

where ω_x^*, ω_y^* and ω_z^* are the components of the vorticity in the x, y and z directions, respectively.

2.2. *Numerical set-up*

We present in figure 1 the cubic computational domain $\mathcal{D}$ selected to perform our numerical simulations. The cubic domain has an edge length of $L_0 = 40$ and is filled with a Newtonian fluid. The angular particle is positioned at (10, 20, 20), with a transversely rotating axis along the z direction. Figure 1 shows the vortex structures identified by the isosurface of $\lambda_2 = -1$ in the wake of a rotating cube with a four-fold rotational symmetry axis (hereafter referred to as RCF4). The negative value of the λ_2-criterion identifies vortex cores as regions where local fluid rotation dominates over strain (Jeong & Hussain 1995). The flow is depicted at $Re = 200$ and $\Omega = 0.3$, with the region of interest highlighted in a pink box. The size disparity between the particle and the computational domain is particularly noticeable. Figure 1 illustrates the octree grid within the three-dimensional computational domain, highlighting the advantages of adaptive mesh refinement in accurately simulating flow dynamics in a large domain that models a quasi unbounded domain. To enhance visualisation, two zoomed views are provided: an

https://doi.org/10.1017/jfm.2025.10292 Published online by Cambridge University Press

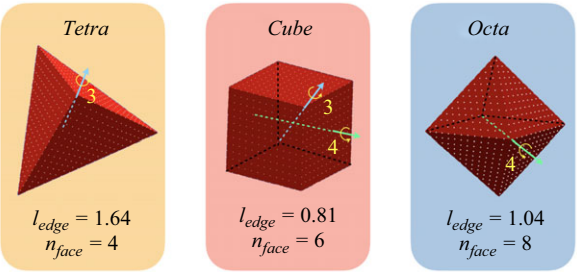

Figure 2. Distribution of Lagrange multipliers (white dots) on the surface of three Platonic polyhedrons (tetrahedron $\phi = 0.67$, cube $\phi = 0.806$ and octahedron $\phi = 0.846$), illustrating their edge lengths (l_{edge}), number of faces (n_{face}) and axis of rotation with their corresponding number of rotational symmetry folds.

x-z cut-plane at $y = 19$ on the right-top panel of figure 1 and a side view of the x-y cut-plane at $z = 20$ on the right-bottom panel, which reveal the high mesh resolution near the surface of the cube as well as in the wake region loaded with vortex structures.

The boundaries of the cubic computational domain are defined as follows: left and right in the x direction, top and bottom in the y direction, and front and behind in the z direction, such that $\Gamma = \text{left} \cup \text{right} \cup \text{top} \cup \text{bottom} \cup \text{front} \cup \text{behind}$. The velocity field $\boldsymbol{u}^*$ satisfies homogeneous Dirichlet boundary conditions on the left, top, bottom, front and behind boundaries. Homogeneous Neumann boundary conditions are imposed on the right boundary and a no-slip condition is imposed on the particle surface ∂P. The complete set of boundary and initial conditions is given by

$$\boldsymbol{u}^*(\boldsymbol{x}^*, t^*) = (U_0^*, 0, 0) \quad \text{on } \Gamma \setminus \text{right}, \tag{2.11}$$

$$\frac{\partial \boldsymbol{u}^*}{\partial x^*}(\boldsymbol{x}^*, t^*) = (0, 0, 0) \quad \text{on right}, \tag{2.12}$$

$$\boldsymbol{u}^*(\boldsymbol{x}^*, t^*) = \boldsymbol{\Omega}^* \times \boldsymbol{r}^* \quad \text{on } \partial P, \tag{2.13}$$

$$\boldsymbol{u}^*(\boldsymbol{x}^*, 0) = (U_0^*, 0, 0) \quad \text{in } \mathcal{D} \setminus P, \tag{2.14}$$

where $\boldsymbol{x}^* = (x^*, y^*, z^*)$ is the position vector.

In the Cartesian octree adaptive grid strategy implemented in Basilisk, a parent cube is subdivided into eight smaller sub-cubes to achieve local mesh refinement in regions of interest (Popinet 2015; Selçuk *et al.* 2021). At each time step, the grid dynamically adapts, refining areas with strong gradient variations in any field of interest while coarsening regions with weak gradient variations. In this study, the flow velocity is the primary field of interest. To accurately model fluid–particle interactions, a phase indicator field is used, taking a value of 0 in the fluid and 1 within the solid particle. This approach ensures that the region near the particle surface is always resolved with the finest grid, allowing precise capture of flow structures in both the boundary layer and the wake region. The hierarchical grid is constructed such that the cell size between successive levels differs by a factor of 2. As a result, the smallest cell size is given by $\Delta x = L_0/2^{n_l}$, where n_l represents the maximum refinement level of the octree grid. In our simulations, the highest level of adaptive mesh refinement (AMR) is chosen as $n_l = 12$, providing sufficient grid resolution with approximately 102 grid points per D_{sph}^*. Additional details on the mesh convergence test can be found in Appendix B.

In this study, we use a collocation point method (Glowinski *et al.* 1999; Wachs *et al.* 2015; Gai & Wachs 2023*a*) within the DLM/FD solver to enforce rigid-body motion constraints on three Platonic polyhedrons, as depicted in figure 2. The point set comprises interior points, which are grid nodes situated inside the particle, as well as surface points.

https://doi.org/10.1017/jfm.2025.10292 Published online by Cambridge University Press

It is shown that the surface of the tetrahedron and of the octahedron consists of triangular faces, while the surface of the cube consists of square faces. The surface points are uniformly distributed parallel to the edges on the particle surface. Despite being isometric, these three angular particles exhibit distinct interaction dynamics with the flow at different angular positions. To investigate the transverse rotation of these particles, we choose several rotation axes with different symmetry fold n_Ω: a three-fold rotational symmetry axis for the tetrahedron (referred to as RTF3), both three-fold and four-fold rotational symmetry axis for the cube (RCF3 and RCF4), and a four-fold rotational symmetry axis for the octahedron (ROF4), as shown in figure 2. For a better resolution of the sharp edges and corners, we strategically place points along all the edges and vertices of the particles. We use a consistent point-to-point distance of $l_{pp} = 2\Delta x$, aligning with the smallest grid cell size around the particle. As the refinement level n_l increases, more surface points are added on the particle. This distribution approach, known as the parallel point set, has been demonstrated to provide satisfactory spatial accuracy (Wachs *et al.* 2015) and can be effectively applied to angular particles (Gai & Wachs 2023*a*,*b*).

As already pointed out earlier in this section, we use the advective time scale $t^*_{ref} = D^*_{sph}/U^*_{ref}$ as the characteristic time scale. In terms of time resolution, the dimensionless time step $\Delta t = \Delta t^*/t^*_{ref}$ is kept below 5×10^{-3} in all our simulations to minimise numerical errors introduced by the operator splitting algorithm. For slowly rotating particles with $\Omega \leqslant 0.1$, the time step is set to $\Delta t = 5 \times 10^{-3}$ to ensure a sufficient number of complete rotation periods for accurate time-averaging at the post-processing level. When $\Omega > 0.1$, a smaller time step of $\Delta t = 5 \times 10^{-4}$ is used to provide enough frames per rotation period, thereby enhancing numerical accuracy and eliminating unphysical oscillations. Additionally, we ensure numerical stability by satisfying the Courant–Friedrichs–Lewy (CFL) condition, which is necessary for the explicit treatment of the advective term in the momentum conservation equation. The time step Δt is dynamically updated according to the following formula:

$$\Delta t = \begin{cases} \min\left(5 \times 10^{-3},\ \min\limits_i \dfrac{0.8\Delta x_i^*}{|\boldsymbol{u}_i^* t_{ref}^*|}\right) & \text{for } \Omega \leqslant 0.1, \\ \min\left(5 \times 10^{-4},\ \min\limits_i \dfrac{0.8\Delta x_i^*}{|\boldsymbol{u}_i^* t_{ref}^*|}\right) & \text{for } \Omega > 0.1. \end{cases} \tag{2.15}$$

In this formula, i denotes a grid cell index and the minimum operator performs over all grid cells. By simulating over a sufficiently long physical time, we ensure that the flow regimes are fully developed. Additional information on the time convergence validation can be found in Appendix B.

3. Flow past a rotating sphere

Prior to discussing the flow past a rotating angular particle, we analyse the behaviour of a rotating sphere in an inertial flow. Figure 3 shows the evolution of the time-averaged drag coefficient $\overline{C_d}$ and lift coefficient $\overline{C_{l,y}}$ for a transversely rotating sphere in flows at $Re = 100$, 300 and 500, with our numerical results depicted by solid lines. Note that the temporal evolution of C_d and $C_{l,y}$ can exhibit oscillatory behaviour due to vortex shedding in the wake. To obtain reliable estimates of $\overline{C_d}$ and $\overline{C_{l,y}}$, we compute their time-averaged values over a sufficiently long period after the transient behaviour has subsided. For a given

https://doi.org/10.1017/jfm.2025.10292 Published online by Cambridge University Press

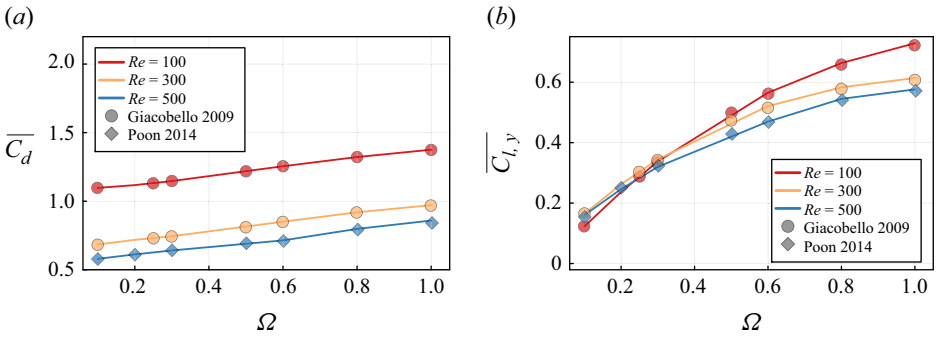

Figure 3. Validation of the evolution of $\overline{C_d}$ and $\overline{C_{l,y}}$ as a function of Ω in the flow past a rotating sphere. The solid lines represent our numerical results at different Reynolds numbers $100 \leqslant Re \leqslant 500$. These results are compared with the data from Giacobello *et al.* (2009) and Poon *et al.* (2014), shown by markers of matching colours.

Re, both $\overline{C_d}$ and $\overline{C_{l,y}}$ increase as the rotation rate Ω varies from 0.05 to 1. In figure 3(*a*), it is shown that $\overline{C_d}$ attains lower values as flow inertia increases from $Re = 100$ to $Re = 500$. Figure 3(*b*) shows that $\overline{C_{l,y}}$ exhibits a clear decreasing trend with Re when $\Omega > 0.25$. The data reported in the literature (Giacobello *et al.* 2009; Poon *et al.* 2014) are presented with scatter points using the colour matching the solid lines for the corresponding $Re = 100$, 300 and 500. Overall, our numerical results are in excellent agreement with those reported in the literature.

4. Flow past a rotating cube

4.1. *Flow regime transition*

We start by presenting an overview of the regimes for 143 simulations of flow past a transversely rotating cube (RCF4) performed in this study. The regime transition map depicted in figure 4 illustrates how the wake structure evolves across the range of rotation rate $0.02 \leqslant \Omega \leqslant 1$ and Reynolds numbers $40 \leqslant Re \leqslant 400$. Flow regimes are represented by colour-coded rectangles, with the upper and lower bounds of Ω clearly marked, offering a visual representation of the flow transitions. We distinguish and discuss the following flow regimes.

(i) Steady vortical regime (SV,): the wake region of the particle displays a steady, typically straight vortical structure.
(ii) Unsteady vortical regime (UV,): the wake flow exhibits unsteady, fragmented vortical structures with irregular sizes.
(iii) Periodic hairpin vortex shedding regime (HS,): the particle wake structure manifests periodic hairpin vortex shedding, maintaining a planar symmetry with respect to the x-y plane passing through the particle centroid.
(iv) Vortex suppression regime (VS,): vortex shedding is suppressed due to the rotation of the particle, where the wake vortical structure becomes straight and steady.
(v) Shear-induced vortex shedding regime (KH,): fluctus vortical structures form in the far-field wake of the particle, arising from Kelvin–Helmholtz instability.
(vi) Double shear-induced shedding regime (DS,): the wake structure exhibits a second shear-induced vortex tail, in addition to the vortical structures caused by Kelvin–Helmholtz instability.

https://doi.org/10.1017/jfm.2025.10292 Published online by Cambridge University Press

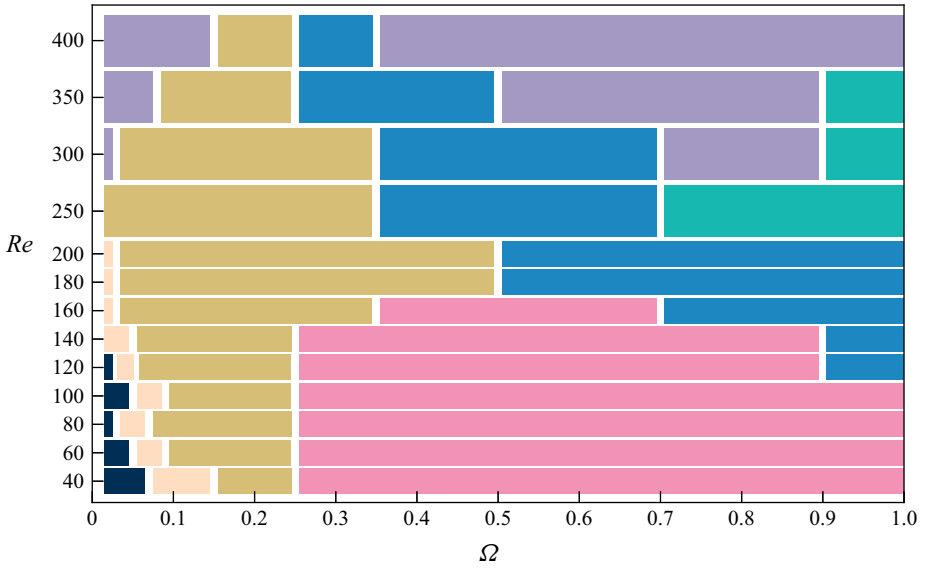

Figure 4. Regime map of the flow past the transversely rotating RCF4 cube at $40 \leqslant Re \leqslant 400$ and $0.02 \leqslant \Omega \leqslant 1$: steady vortical (SV,), unsteady vortical (UV,), periodic hairpin vortex shedding (HS,), vortex suppression (VS,), shear-induced shedding (KH,), double shear-induced shedding (DS,) and chaotic shedding (CS,) regime.

(vii) Chaotic shedding regime (CS,): the wake structure becomes unpredictable and irregular, losing its planar symmetry and exhibiting chaotic vortex shedding due to the increased fluid inertia.

At very low rotation rate, $\Omega = 0.02$, the flow past a rotating cube undergoes a sequence of regime transitions as Re increases: SV, UV, HS and ultimately CS at high Re. At low flow inertia $Re = 40-100$, slow particle rotation $\Omega \leqslant 0.2$ promotes the formation of vortical structures and their periodic shedding in the particle wake. As the rotation rate increases to $\Omega = 0.3$, vortex shedding in the particle wake is suppressed, marking the onset of the VS regime. With increasing flow inertia, the suppressed wake structure becomes unsteady at high rotation rates due to the K-H instability, a phenomenon caused by velocity shear between the particle wake and the bulk flow. The KH regime emerges at $Re = 120$ and $\Omega = 1$. From $Re = 160$ to $Re = 200$, both the HS and KH regimes expand, gradually replacing the VS regime in the range $0.3 \leqslant \Omega \leqslant 0.8$. At $Re = 250$ and $\Omega = 0.8$, a second shear-induced vortex tail appears in the upper wake, marking the onset of the DS regime. Beyond $Re = 250$, the HS, KH and DS regimes are superseded by the CS regime due to the increased flow instability. At $Re = 400$, the flow past a rotating cube still exhibits periodic, organised wake structures in the HS and KH regimes at $\Omega = 0.2$ and 0.3, while all other cases transition to chaotic behaviour. Overall, we observe that a moderate rotation rate, particularly in the range of $\Omega = 0.2 \sim 0.4$, either stabilises or reorganises the wake: at low Re, it leads to vortex suppression, while at high Re, it restructures the wake into periodic shedding within a highly unsteady flow.

4.2. *Vortex generation on the cube*

4.2.1. *Slowly rotating cube*

To better understand the regime transitions and wake stability in the flow past a transversely rotating cube, it is important to first clarify the mechanism of vortex

https://doi.org/10.1017/jfm.2025.10292 Published online by Cambridge University Press

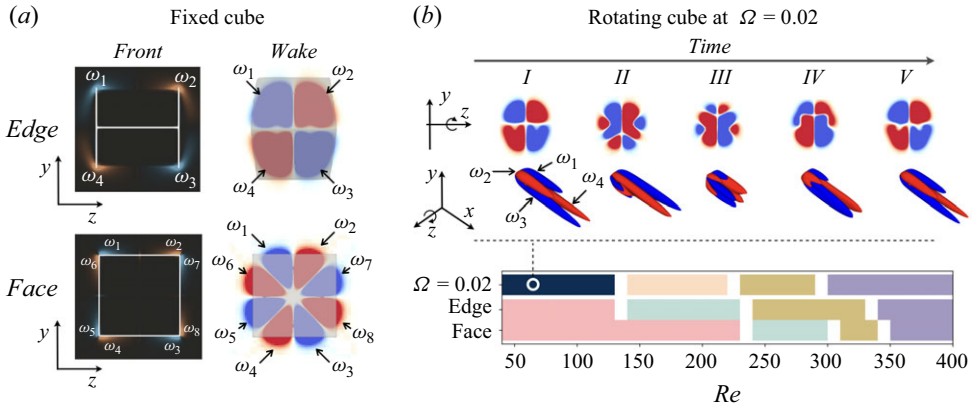

Figure 5. Vortex generation mechanism on the surface and in the wake of the slowly rotating RCF4 cube. (*a*) Schematic of vortex generation on the front surface (left subpanels with black backgrounds) and in the wake of fixed cubes (right subpanels with white backgrounds), with one edge and one face facing the incoming flow (x^+ direction). In all subpanels, red and blue regions indicate positive and negative ω_x, respectively. (*b*) Regime transition sequence for a slowly rotating cube at $Re = 60$ and $\Omega = 0.02$, compared with the regime transition in the flow past a fixed cube with an edge or a face facing the flow. The temporal evolution of the vorticity pattern ω_x in the particle wake is illustrated, along with side views of the isosurfaces $\omega_x = \pm 0.03$.

generation on the cube. In the RCF4 configuration, the transversely rotating cube has two primary angular positions: one with a face directly facing the incoming flow and the other with an edge (dividing two front faces) facing the flow. We consider an extreme case where the cube is fixed in the flow at these two angular positions and illustrate the corresponding streamwise vorticity ω_x generation in figure 5(*a*). Here, the choice of ω_x is motivated by its higher sensitivity to wake structure evolution, enabling more accurate and precise characterisation of the wake dynamics (Gai & Wachs 2023*a*).

As thoroughly discussed in our previous work (Gai & Wachs 2023*d*), an inclined front face of the fixed angular particle generates a pair of counter-rotating streamwise vortices ω_x. For example, when the cube has an edge facing the flow, one pair of vortices (ω_1, ω_2) forms on the upper front face, while a second pair (ω_3, ω_4) forms on the lower front face. These two vortex pairs are then advected into the wake of the cube, maintaining a typical pattern of two vortex pairs (shown in blue and red) as depicted in figure 5(*a*). When a square face of the cube is oriented perpendicular to the flow, four pairs of oppositely signed streamwise vortices are generated. In addition to the two pairs formed on the upper and lower faces of the cube, two more vortex pairs appear on the side faces: the pair (ω_5, ω_6) on the left side face and the pair (ω_7, ω_8) on the right face. Although these side vortex pairs are also generated in the edge facing the flow configuration, their intensity is significantly lower and much less visible compared with the vortices produced on the upper and lower faces.

Now, we rotate the cube slowly at $\Omega = 0.02$ around the z-axis to observe how the vorticity pattern in the particle wake evolves with time. In figure 5(*b*), we present several snapshots of the temporal evolution of the ω_x pattern in the y-z plane at $x = x_p + 1.5$ (x_p denotes the x coordinate of the particle centroid) for the case at $Re = 60$ in the upper panel. The side views of the isosurface $\omega_x = \pm 0.03$ are illustrated in the bottom of the upper panel for better clarity. In the SV regime, the ω_x patterns are planar and symmetric, exhibiting a high similarity to those in the fixed edge cube case shown in figure 5(*a*). The two pairs of streamwise vortices are clearly visible in the side view. We know that in the case of a fixed edge cube in the multi-axis steady symmetry regime (MSS,), the

https://doi.org/10.1017/jfm.2025.10292 Published online by Cambridge University Press

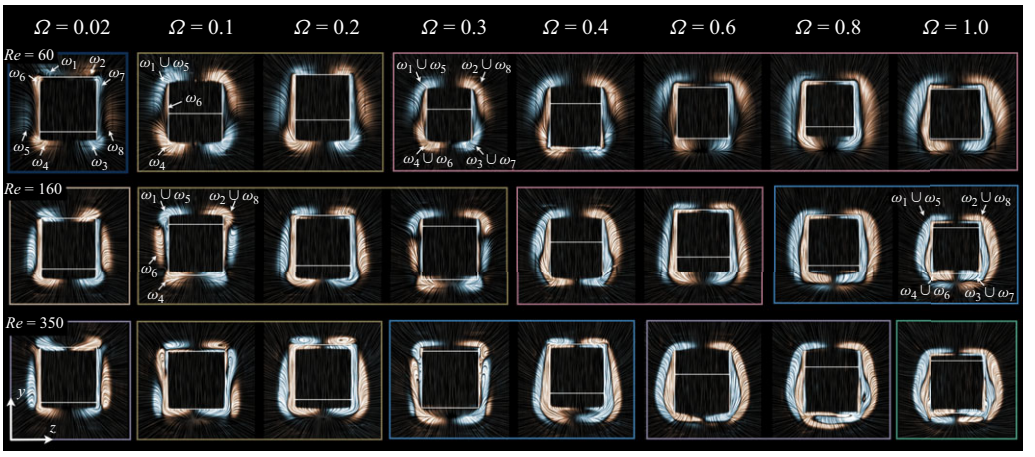

Figure 6. Visualisation of vortex merging on the front surface of the rotating RCF4 cube in the y-z plane at $x = x_p - 0.1$, with red and blue regions representing positive and negative ω_x, respectively. Flow streamlines are included to enhance the visualisation of the wake vortices. The various flow regimes are highlighted in colour-coded boxes, and the cube projected outline on the y-z plane is sketched for reference.

four vortex filaments in the wake are of equal length and remain steady. With transverse rotation, the length of the vortex pairs evolves in time. The length of the vortex pair (ω_1, ω_2) is clearly shorter than that of the vortex pair (ω_3, ω_4) in the first snapshot I. In snapshot II, the upper vortex pair (ω_1, ω_2) becomes longer instead. In the following, we will demonstrate how the reciprocal motion of vortex pairs and the evolution of their relative strength can explain the vortex suppression.

The similarity between the slowly rotating cube and a fixed edge cube can also be observed from the regime map. In the lower panel of figure 5(b), we present the regime map of flow past an edge and a face cube for $Re = 40-400$. In place of the SV and UV regimes, the fixed cube exhibits the MSS (▬) and the planar steady symmetry regime (PSS, ▬), respectively. It is evident that the regime transition sequence of the slowly rotating cube shows very similar critical Re for the first two regime transitions as those observed for the fixed edge cube, rather than those observed for the fixed face cube. At higher Re, rotation causes flow instability to occur earlier (at $Re = 300$) compared with the fixed edge cube (at $Re = 340$).

4.2.2. *Vortex merging induced by rotation*

Unlike the multi-axis symmetry typically observed in the wake of a fixed cube, the particle rotation promotes the merging of surface vortices, resulting in a planar symmetry of vortex distribution, even at low Reynolds numbers such as $Re = 60$. The merging process occurs once the vortices are generated on the front surface of the cube. In figure 6, we present the ω_x distribution in the y-z plane at $x = x_p - 0.1$ for flows at $Re = 60$, 160, 350 and $\Omega = 0.02-1$. We highlight the vortex cores by setting the colour bar to $\omega_x \in [-1, 1]$, where regions with higher magnitude of ω_x are represented by red and blue, while areas with values close to 0 appear in black.

In the case of $Re = 60$ and $\Omega = 0.02$, we observe the generation of four pairs of streamwise vortices ($\omega_1 - \omega_8$) similar to the fixed cube case in figure 5(a). Under the cube rotation in figure 6, the two side vortices ω_5 and ω_8 are fairly weak and get pushed away from the cube surface by their opposite-signed counter-parts ω_6 and ω_7, respectively. This gives room for the vortex ω_6 to spread on the left side of the cube and to reach its arm to its neighbour of the same positive sign, the stronger ω_4 generated by the lower face.

https://doi.org/10.1017/jfm.2025.10292 Published online by Cambridge University Press

We observe the same mechanism between ω_7 and ω_3. This process depicts the initiation of the surface vortex merging $\omega_4 \cup \omega_6$ and $\omega_3 \cup \omega_7$ that play key roles in the wake stability of the rotating cube. With the increase of the rotation rate, at $Re = 60$ and $\Omega = 0.1$, we observe that the weak side vortices ω_5 and ω_8, which are pushed away from the side faces, find their way to reach their neighbours of the same sign, ω_1 and ω_2 from the upper face, respectively. A second merging process takes place on the top of the cube, but slightly away from the surface, resulting in the vortex structure $\omega_1 \cup \omega_5$ and $\omega_2 \cup \omega_8$ as depicted at $Re = 60$ and $\Omega = 0.3$. We note that all the investigated cases exhibit these two types of rotation-induced vortex merging processes on the cube front surface, resulting in an inner pair and an outer pair of streamwise vortices propagating to the wake.

It is worth mentioning that some variations of the merging process may occur. At low rotating rate, such as $\Omega = 0.02$, we observe that the merging of the outer vortex may not happen, this is visible in the cases $Re = 160$ and $Re = 350$ in figure 6. In the HS regime, the periodic vortex shedding takes place, and we note that the roles of the inner and outer vortex pairs can swap in time. For instance, in the snapshot of the case at $Re = 160$ and $\Omega = 0.1$, the merged vortex $\omega_1 \cup \omega_5$ appears on the cube surface while vortex ω_6 is pushed away to meet ω_4, due to the larger inclination angle of the upper face. As the cube continues to rotate, we see that the merged vortex $\omega_1 \cup \omega_5$ moves aways from the side face, while the merged vortex $\omega_4 \cup \omega_6$ returns to the surface, similar to the snapshot at $Re = 60$ and $\Omega = 0.1$. With the increase of the rotation rate, $\Omega \geqslant 0.4$, the impact of the cube angular position diminishes, and the alternating role swap ceases. The merged vortices $\omega_4 \cup \omega_6$ and $\omega_3 \cup \omega_7$ consistently form the inner pair, as observed in the KH regime at $Re = 160$, $\Omega = 0.8$ and $\Omega = 1$. In the CS regime, even though the planar symmetry is broken on the front surface, the merging process still follows the same mechanism, as shown in the case $Re = 350$ and $\Omega = 0.8$ in figure 6.

4.2.3. *Near-wake vortex structures*

Now that we clarified the vortex generation and merging process, we present in figure 7 the ω_x distribution in the particle wake region in the y-z plane, right next to the rear face at $x = x_p + 0.6$. At this point, the interaction between the vortices and the particle surface terminates. The evolution of the wake structure is driven solely by fluid dynamics and vortex interactions. Four Reynolds numbers ($Re = 60{-}350$) are selected to illustrate the wake vortices across the seven flow regimes studied. The same colour scale ($\omega_x \in [-1, 1]$) as that used in figure 6 is used for consistency and better comparison. Regions in red and blue indicate higher vorticity magnitude, while black areas represent lower vorticity magnitude. In the case $Re = 60$ and $\Omega = 0.02$, the vortex pattern appears blurred due to the low vortex strength.

At low flow inertia, $Re = 60$, the merged vortex pairs near the cube surface, ω_{46} (hereafter denoting the merged vortex $\omega_4 \cup \omega_6$) and ω_{37} (hereafter denoting the merged vortex $\omega_3 \cup \omega_7$), exhibit dominant magnitudes and maintain symmetry with respect to the x-y plane across the cube centroid. A higher Ω enhances ω_x, particularly in the VS regime, highlighted by the pink box in the first row of figure 7. In this regime, periodic vortex shedding is suppressed by the cube rotation, resulting in a steady vorticity distribution that only includes the vortex pairs ω_{46} and ω_{37}, as seen in the case $Re = 60$ and $\Omega = 0.6$. At $Re = 160$ and $Re = 250$, particularly in the UV and HS regimes, we observe the formation of the outer vortex pairs ω_{15} and ω_{28}, originating from the upper front surface of the cube, as shown in the cases at $\Omega = 0.3$. In the HS regime, the periodic interactions between the inner and outer vortex pairs result in a variety of vorticity distribution patterns, as illustrated in figure 7.

https://doi.org/10.1017/jfm.2025.10292 Published online by Cambridge University Press

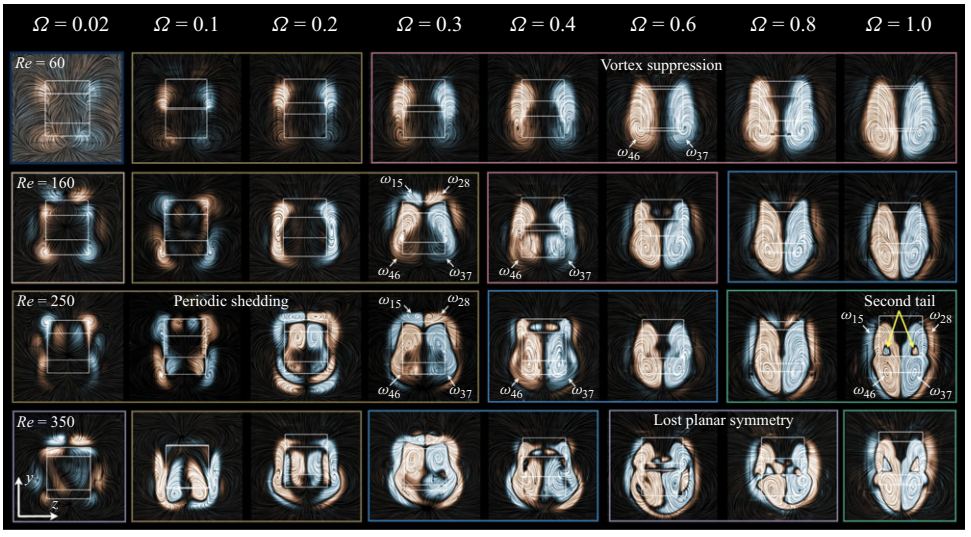

Figure 7. Visualisation of vortex pair generation near the rear surface of the rotating RCF4 cube in the y-z plane at $x = x_p + 0.6$, with red and blue regions representing positive and negative ω_x, respectively. Flow streamlines are included to enhance the visualisation of the wake vortices. The various flow regimes are highlighted in colour-coded boxes, and the projected outline of the cube on the y-z plane is sketched for reference.

At $Re = 160$, increasing the rotation rate to $\Omega = 0.4$ results in relatively weak outer vortex pairs ω_{15} and ω_{28}, as they are pushed away from the wake, marking the onset of the VS regime. In the KH regime indicated by the blue box, at $\Omega = 0.8$ and $\Omega = 1$, the magnitude of ω_{15} and ω_{28} increases again, and they tightly wrap around the inner vortex pair like tulip petals. A similar vorticity pattern is also observed in the DS regime at $Re = 250$ and $Re = 350$, as shown in the green box in figure 7. In the DS regime, a second shear-induced vortical tail forms in the wake, with the vortex cores of this second tail clearly visible at $\Omega = 1$ for both $Re = 250$ and $Re = 350$. Overall, the near-wake vortex structure maintains a planar or pseudo-planar symmetry with respect to the x-y plane, except in cases within the CS regime.

In summary, the generation and merging of vortex pairs on the particle surface dictate the near-wake vortex patterns, which in turn influence the formation, dynamics and stability of the wake vortical structures, thereby shaping the flow regimes. Our findings demonstrate that the formation of two vortex pairs – inner and outer – is a universal process across all flow regimes within the investigated parameter space.

4.3. *Wake vortical structures*

Once formed at the particle surface, the streamwise vortices are advected into the wake region, where they develop into complex vortical structures. In the following sections, we will closely examine the interactions between these wake structures, with a focus on gaining new insights into how the sharp edges of the cube influence wake flow instability.

4.3.1. *Vortex shedding and suppression*

We recall that behind a transversely rotating sphere, the particle rotation amplifies wake unsteadiness, leading to periodic hairpin vortex shedding at lower critical Re compared with a fixed sphere. This shedding follows a characteristic build-up and release process. As Ω increases, the vortices in the recirculation region disappear, and vortex shedding is suppressed within $0.3 \leqslant \Omega \leqslant 0.5$ for $Re = 100$–300 (Giacobello *et al.* 2009). Beyond this

https://doi.org/10.1017/jfm.2025.10292 Published online by Cambridge University Press

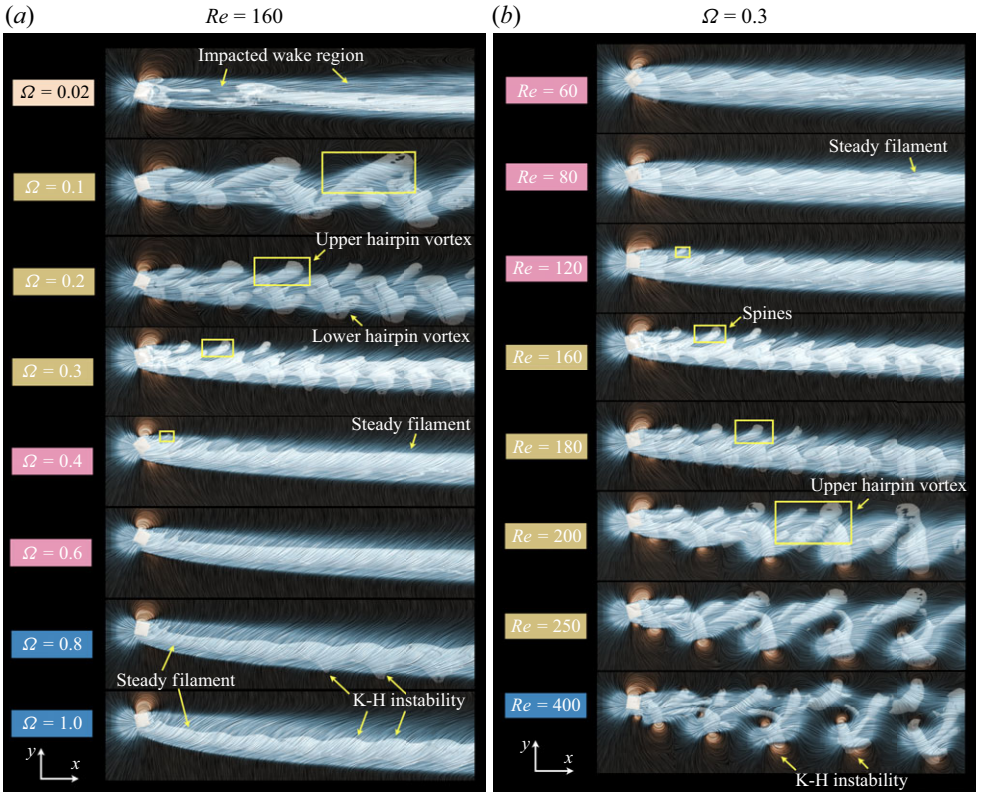

Figure 8. Vortical structures identified by $\lambda_2 = -1$ in the wake of the rotating RCF4 cube (*a*) at $Re = 160$ and (*b*) at $\Omega = 0.3$ in the x-y plane. The red and blue regions indicate positive and negative disturbed velocity, $\tilde{u}_x \in [-0.1, 0.1]$, respectively. Flow streamlines based on $\tilde{\boldsymbol{u}}$ are plotted to enhance the clarity of the wake flow field. The different flow regimes are distinguished by colour-coded boxes on the left of each subpanel.

suppression, at higher values of both Ω and Re, the steady vortical tail becomes unsteady once again, driven by a Kelvin–Helmholtz instability.

How different are the wake structures of a rotating angular particle compared with those of a rotating sphere? To investigate this, we present snapshots of the vortical structures behind a rotating cube in the x-y plane, as shown in figure 8. The vortex structures are identified using the isosurface $\lambda_2 = -1$. Due to the dominance of the streamwise incoming velocity over the other velocity components, important details of the wake region may be obscured. To better capture the wake dynamics, we plot the streamlines of the disturbed flow velocity $\tilde{\boldsymbol{u}} = (\boldsymbol{u}^* - U^*_{ref}\boldsymbol{e_x})/U^*_{ref}$ and colour these streamlines using the scale of $\tilde{u}_x \in [-0.1, 0.1]$, to reveal more details of the wake region.

As an example, figure 8(*a*) illustrates the evolution of wake structures with increasing rotation rates $0.02 \leqslant \Omega \leqslant 1$ at $Re = 160$. The flow regime transitions from UV to HS, VS and eventually KH, following a sequence similar to that observed for a sphere. At $\Omega = 0.02$, the wake behind the rotating cube appears straight, with fragmented vortical structures shed from the cube at a low frequency. Beneath the vortical structures, a broad, elongated strip region ($\tilde{u}_x \leqslant 0$) is visible in light blue, extending behind the cube. This impacted wake region, present in all subpanels of figure 8, encloses the wake vortical structures and defines the boundary of the disturbed wake flow. As the rotation rate increases to $\Omega = 0.1$–0.3, hairpin vortex shedding occurs with increasing frequency.

https://doi.org/10.1017/jfm.2025.10292 Published online by Cambridge University Press

A notable difference from the rotating sphere case is that the vortex shedding frequency behind a rotating cube is significantly higher at the same Re and Ω. Two distinct types of vortex structures are observed: upper hairpin vortices originate from the upper front face of the rotating cube, while lower hairpin vortices emerge from the lower front face and side faces. Compared with $\Omega = 0.2$, the wake vortex structures become smaller at $\Omega = 0.3$. In the highlighted yellow rectangles, it is clear that the size of the upper hairpin vortices decreases with increasing Ω, disappearing entirely at $\Omega = 0.4$, where wake vortex shedding is suppressed and manifests as a steady filament. Some residual bumpy structures remain near the top rear face of the cube at $\Omega = 0.4$, but they vanish completely at $\Omega = 0.6$. At higher rotation rates, the fluctus structures resulting from the Kelvin–Helmholtz instability are observed along the steady filaments near the lower boundary of the impacted wake region at $\Omega = 0.8$ and $\Omega = 1$.

In terms of flow inertia, we present the evolution of wake vortical structures in the x-y plane at the same $\Omega = 0.3$ while varying the Reynolds number in the range $60 \leqslant Re \leqslant 400$ in figure 8(b). We focus on the influence of flow inertia on wake instability, particularly in cases where vortex shedding is suppressed in the VS regime. At $Re = 60$ and $Re = 80$, the λ_2 isosurface shows bumpy structures near the rear surface of the cube, but it stabilises into a steady filament in the far-wake region of the cube; this is not the case at $\Omega = 0.2$ and the same Re. Thus, we classify these cases in the VS regime, where vortex suppression is effective. As Re increases, vortex shedding reemerges, and the size of the vortical structures grows with Re. At $Re = 120$, small spine-like structures appear along the top boundary of the impacted wake region near the cube rear surface, highlighted in yellow rectangles in figure 8(b). As Re increases, the spine structures grow in size and gradually evolve into upper hairpin vortices, as depicted in the HS regime at $Re = 200$. This process reverses the vortex suppression highlighted in the yellow rectangles in figure 8(a). Specifically, the spines (or upper hairpin vortices) generated by the upper front face of the rotating cube are suppressed as Ω increases, but as flow inertia rises, these vortices reemerge through a reversed yet similar mechanism. Between $Re = 180$ and $Re = 200$, the vortex shedding frequency noticeably decreases and remains constant up to $Re = 400$. At this point, the hairpin vortical structures become more complex, while still maintaining periodicity and symmetry about the x-y plane.

From figure 8, it is clear that the sharp edges of the rotating cube, particularly those on the upper front face, play a critical role in both the suppression and reemergence of vortex shedding. These edges strongly influence the generation of vortices, which in turn drive flow instabilities through their interactions in the wake region. To better understand these interactions, we examine the evolution of streamwise vortex pairs ω_x in the x-z plane, visualised by isosurfaces at $\omega_x = \pm 0.03$ (with red indicating positive ω_x and blue indicating negative ω_x) for $40 \leqslant Re \leqslant 200$ and $0.1 \leqslant \Omega \leqslant 0.8$ in figure 9. Our analysis focuses on the case at $\Omega = 0.3$ and $Re = 120$, while reducing the transparency of other cases for enhanced clarity.

The flow past a rotating cube generates alternating vortex pairs of opposite sign in the x-z plane. As discussed in figure 7, one vortex pair, consisting of ω_{15} and ω_{28}, originates from the upper front face of the cube and is located in the upper region of the wake (relative to the y-axis). The other pair, ω_{46} and ω_{37}, forms from the merging of vortices generated by the lower front and side faces, and resides in the lower region of the wake. These two vortex pairs are shed alternately into the wake, as highlighted in yellow at $Re = 120$ and $\Omega = 0.3$ in figure 9.

Considering $Re = 120$, at a low rotation rate $\Omega = 0.1$, the size of the upper vortex pair (ω_{15}, ω_{28}) is comparable to that of the lower vortex pair (ω_{46}, ω_{37}), leading to a standard periodic hairpin vortex shedding. As Ω increases, with the rotation vector aligned along

https://doi.org/10.1017/jfm.2025.10292 Published online by Cambridge University Press

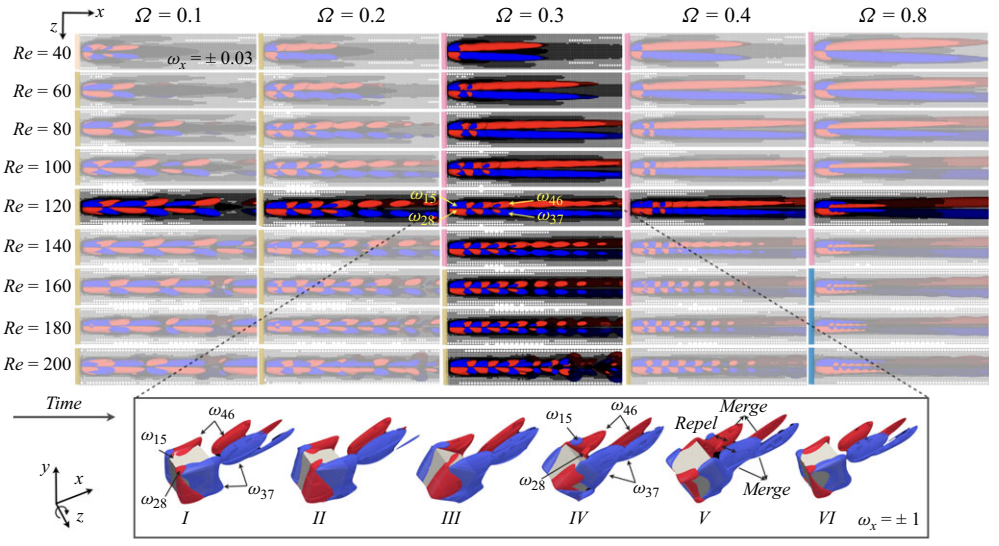

Figure 9. Evolution of streamwise vortex pairs identified by isosurfaces of $\omega_x = \pm 0.03$ (red for positive ω_x and blue for negative ω_x) in the x-z plane. Lower panel shows snapshots of temporal evolution of the core of the vortex pairs identified by $\omega_x = \pm 1$ within a single rotation period.

the z-axis, the first direct effect is a reduction in fluid–particle relative velocity on the upper side (y^+) of the cube, while the relative velocity on the lower side (y^-) increases (within the range $\Omega \leqslant 1$ in this study). This weakens the upper vortex pair (ω_{15}, ω_{28}) while strengthening the lower vortex pair (ω_{46}, ω_{37}). Another key point is that, during each rotation period, four faces of the cube contribute to the generation of the upper vortex pair, with each face producing one. These faces are referred to as effective faces, and their number, denoted as $N_{\mathcal{F}}$, depends on the particle shape and the axis of rotation. The effective faces directly determine the primary shedding frequency of the vortex pairs, which is typically proportional to $N_{\mathcal{F}}$, a distinctive feature of rotating angular particles. Hence, with Ω increasing from 0.1 to 0.2 in the HS regime, the shedding frequency doubles. As a result of these combined effects, at $\Omega = 0.3$, the lower vortex pair shedding becomes more frequent and stronger, resulting in vortex merging in the wake. In the upper wake, the upper vortex pair is too weak to pinch off its lower counterpart. This imbalance results in a long, steady vortical tail with two filaments in the VS regime, explaining the vortex suppression, which persists up to $\Omega = 1$ at $Re = 120$.

In the lower panel of figure 9, we present six snapshots of the vortex pair shedding process over a single rotation period for the flow at $Re = 120$ and $\Omega = 0.3$, shown from a side view. The positions of the upper and lower vortex pairs are indicated. To improve the clarity of the visualisation, the vorticity isosurface criterion has been increased to $\omega_x = \pm 1$ to better highlight the vortex cores. At $\Omega = 0.3$, the upper vortex pair (ω_{15}, ω_{28}) is clearly weaker than the lower vortex pair (ω_{46}, ω_{37}), as seen in snapshot I. As the cube keeps rotating, snapshots IV and V show the interaction between the upper and lower vortex pairs. Due to their opposite signs, ω_{15} and ω_{46} repel each other in space, as do ω_{28} and ω_{37}. In snapshots V and VI, the upper vortex pair is pushed away and dissipates due to diffusion, while the two successive lower vortex pairs begin to merge. The presence of the weak upper vortex pair acts as wedges on the strong lower pair isosurface and leads to the formation of the spine structures observed in figure 8. As Re increases, the upper vortex pairs strengthen and grow in size, significantly influencing the wake stability.

https://doi.org/10.1017/jfm.2025.10292 Published online by Cambridge University Press

At $Re = 160$, their increased presence becomes substantial enough to prevent the merging of the lower vortex pairs, thereby leading to the HS regime. Consequently, the reemergence of periodic vortex shedding follows the same mechanism as previously discussed, but in reverse.

In summary, our results provide a clear explanation for vortex suppression and reemergence mechanism through the lens of vortex interaction. The alternating shedding of upper and lower vortex pairs characterises the periodic hairpin vortex formation, while the merging of the lower vortex pair is the primary mechanism behind vortex suppression. The weakened upper vortex pairs are responsible for the formation of spine structures in the wake. Compared with the smooth geometry of a sphere, the sharp edges and distinct faces of the rotating cube provide a clearer understanding of the roles played by the upper and lower vortex pairs in these processes.

4.3.2. *Wake structures in high-Re regimes*

A remarkable feature of the flow past an angular particle is the wide variety of vortex shedding patterns that form in the wake. At high flow inertia, specifically when $Re \geqslant 250$, the rotation of the cube introduces new dynamics in the wake structures, leading to distinct flow regimes. In figure 10, we present snapshots of these complex vortical structures and shedding patterns for $Re \geqslant 250$ in the x-y plane. The streamlines of the disturbed velocity field $\tilde{\boldsymbol{u}}$ are drawn to provide a clearer depiction.

At $Re = 250$, as shown in figure 10(a), vortices follow a classical periodic hairpin vortex shedding pattern in the HS regime for $0.02 \leqslant \Omega \leqslant 0.3$. While the shedding frequency generally increases with Ω, a slight decrease is observed between $\Omega = 0.2$ and $\Omega = 0.3$. Interestingly, at $\Omega = 0.2$, the upper and lower vortex pairs, which are similar in size, are shed in phase, leading to a double-symmetric hairpin vortex shedding (DHS regime), resembling the pattern observed in the flow past an edge tetrahedron (Gai & Wachs 2023*b*). At $\Omega \leqslant 0.3$, the impacted wake region ($\tilde{u}_x \leqslant 0$) no longer appears as a wide strip, instead displaying blue regions tightly surrounding the vortical structures. As Ω increases, the flow transitions to the KH regime, and the impacted wake region once again takes on a long strip shape. In this regime, the upper vortex pairs are moderated by mechanisms discussed earlier but are not fully suppressed. The lower vortex pairs, due to high fluid inertia, are unable to merge. At $\Omega = 0.4$ and $\Omega = 0.6$, we observe the formation of fluctus at the lower boundary of the impacted wake region, where red zones indicate the part of streamwise acceleration of the vortex cores. It is evident that the shedding frequency of the shear-induced vortices is higher than that of the vortices released from the recirculation region at $\Omega = 0.3$. As Ω increases further, the shear-induced vortex shedding stabilises at $\Omega = 0.8$ and $\Omega = 1$. Interestingly, under high rotation rates, the upper vortex pairs become enhanced and tend to merge, forming a steady, elongated structure – referred to as the second tail – at $Re = 250$ and $\Omega = 1$. Note that this secondary tail is located at the upper boundary of the impacted wake region, which also contains two filaments symmetric to the x-y plane. The emergence of the secondary tail marks the onset of the DS regime. Due to the interplay of the flow inertia and angular particle rotation, we obtain a steady flow at relatively high Re and Ω.

Figure 10(b) presents the vortex shedding pattern at $Re = 300$, where the CS regime kicks in. Even when the cube slowly rotates at $\Omega = 0.02$, the wake vortex distribution behind the cube is no longer planar symmetric. As Ω increases, the wake structure reorganises and the HS regime is observed for $0.1 \leqslant \Omega \leqslant 0.3$. Especially, the double-hairpin shedding is also observed for $Re = 300$ and $\Omega = 0.2$. With further increase of Ω, we note that the shear-induced shedding becomes predominant at $\Omega = 0.4$ and

https://doi.org/10.1017/jfm.2025.10292 Published online by Cambridge University Press

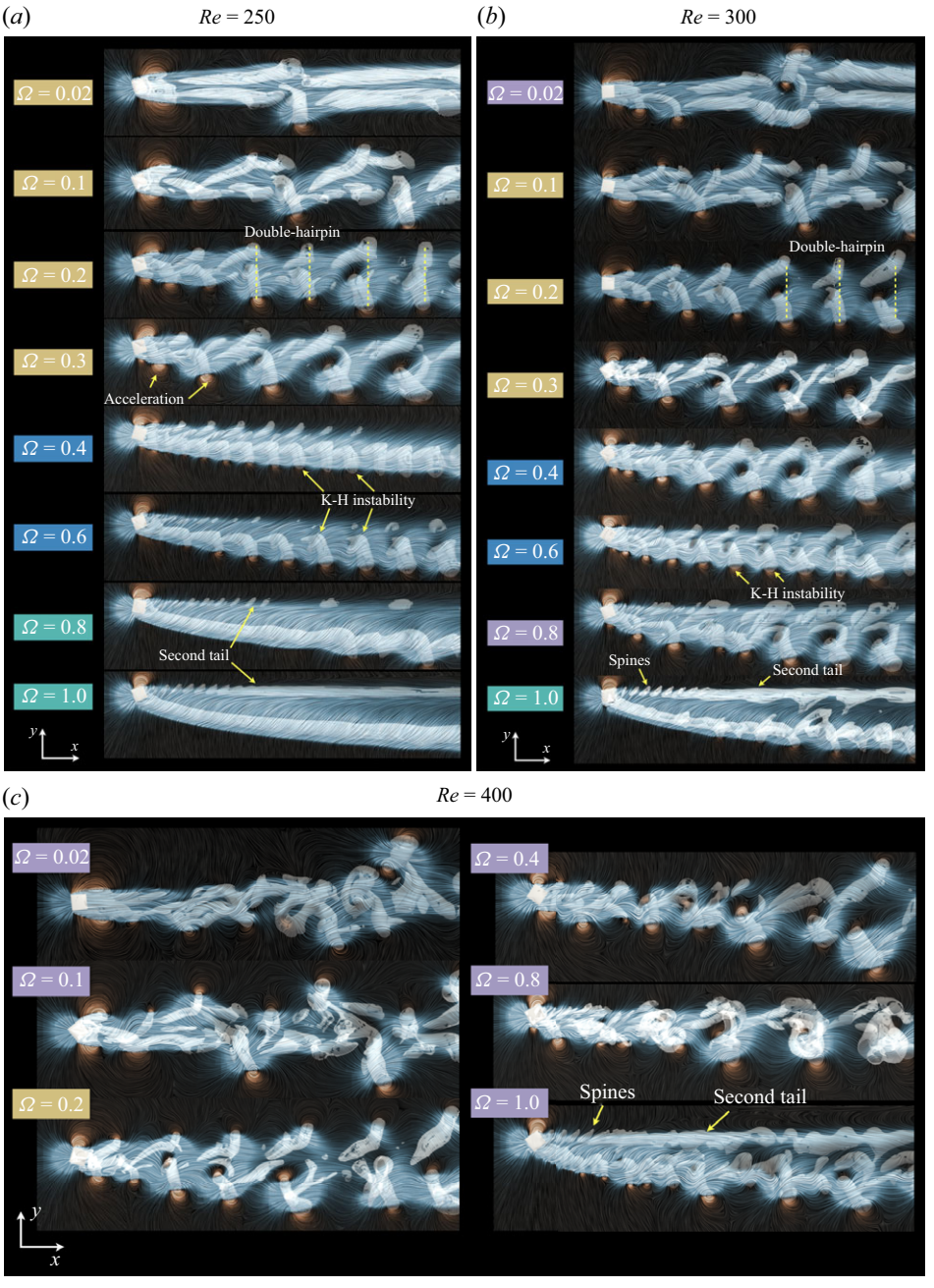

Figure 10. Vortical structures identified by $\lambda_2 = -1$ in the wake of the rotating RCF4 cube at (*a*) $Re = 250$, (*b*) $Re = 300$ and (*c*) $Re = 400$. The red and blue regions indicate positive and negative disturbed velocity, $\tilde{u}_x \in [-0.1, 0.1]$, respectively. Flow streamlines based on $\tilde{\boldsymbol{u}}$ are plotted to enhance the clarity of the wake vortex patterns. The different flow regimes are distinguished by colour-coded boxes, corresponding to each rotation rate.

https://doi.org/10.1017/jfm.2025.10292 Published online by Cambridge University Press

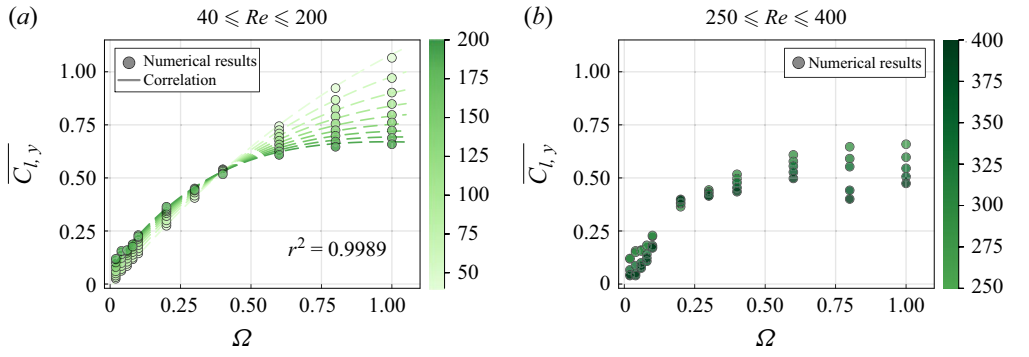

Figure 11. (*a*) Evolution of the time-averaged lift coefficient $\overline{C_{l,y}}$ of the rotating RCF4 cube as a function of Ω at $40 \leqslant Re \leqslant 200$ with increment $\Delta Re = 20$. Our numerical simulation results (coloured circles) are compared with the empirical correlation proposed in (4.1) (dashed lines). (*b*) Evolution of $\overline{C_{l,y}}$ at higher Reynolds numbers, $250 \leqslant Re \leqslant 400$ with increment $\Delta Re = 50$. Darker circles indicate higher values of Re.

$\Omega = 0.6$. The upper vortex pairs are much enhanced by the flow inertia compared with the case $Re = 250$ in figure 10(*a*). At $\Omega = 0.8$, the interaction between the upper and lower vortices becomes irregular, eliminating planar symmetry. Interestingly, at $\Omega = 1$, the planar symmetry is restored and the DS regime emerges. However, both tails at the upper and lower boundaries of the impacted wake region become unsteady. At $Re = 400$, as shown in figure 10(*c*), the wake structure loses its periodicity in the CS regime, except at $\Omega = 0.2$ and 0.3. Compared with the wake patterns observed at $Re = 250$ and 300, the impacted wake region at $\Omega = 1$ is less inclined and more aligned with the cube. Although a second tail is still present, the vortex shedding pattern becomes fully chaotic and irregular.

To offer readers a more in-depth understanding of vortex shedding, suppression and wake instability, the wake structures in the flow past a rotating cube in the x-y plane are presented for additional selected cases in Appendix C.

4.4. *Hydrodynamic forces on the cube*

The previous analysis offers new insights into the dynamics of vortical structures in the wake of a rotating cube. As these vortices form and shed, they induce changes to the velocity and pressure fields, and these changes significantly impact the lift and drag forces. We now turn our attention to the hydrodynamic forces exerted by the surrounding fluid on the particle.

4.4.1. *Magnus effect and lift coefficient*

We know that the flow interaction with the cube is predominantly influenced by two factors: the flow inertia Re and the rotation rate Ω. To quantitatively assess the impact of these factors, we plot the evolution of the time-averaged lift coefficient, $\overline{C_{l,y}}$, as a function of Ω for $40 \leqslant Re \leqslant 200$, as shown in figure 11(*a*). For higher flow inertia ($Re \geqslant 250$), the evolution of $\overline{C_{l,y}}$ is presented separately in figure 11(*b*), using the same colour bar for clarity. To ensure accurate temporal averaging, $\overline{C_{l,y}}$ is computed over a sufficiently long period once the flow has fully developed.

In general, increasing Ω results in a higher lift force due to the enhanced Magnus effect. The rotation of the cube causes a direct deceleration of the flow velocity on the bottom side (y^-) compared with the top side (y^+). According to Bernoulli's principle, the higher velocity on the top corresponds to lower pressure, while the lower velocity on the bottom creates higher pressure, generating lift pointing to the y^+ direction. At low

https://doi.org/10.1017/jfm.2025.10292 Published online by Cambridge University Press

flow inertia, such as $Re = 40$, $\overline{C_{l,y}}$ increases almost linearly with Ω. With the increase of inertia, however, the increase in $\overline{C_{l,y}}$ becomes constrained, causing the curves to bend downward in figure 11(a). The influence of Re on $\overline{C_{l,y}}$ can be divided into two parts: for $\Omega \leqslant 0.4$, the effect of Re is small and tends to enhance $\overline{C_{l,y}}$; for $\Omega > 0.4$, higher Re leads to a lower $\overline{C_{l,y}}$. A possible explanation is that the enhanced flow unsteadiness results in reducing the pressure difference between the top and bottom surfaces of the rotating cube, thereby diminishing the Magnus effect. Between $\Omega = 0.3$ and $\Omega = 0.4$, we find a critical regime transition region where all the data points exhibit a very close value of $\overline{C_{l,y}}$. In this region, the rotation-driven time scale becomes smaller than the vortex formation time scale. We observe the complete suppression of vortex shedding and a reorganisation of the wake. The wake flow fully transitions from the HS regime to the VS regime (KH regime for $Re = 180$ and $Re = 200$), as shown in figure 4. An extraordinary property of $\Omega = 0.4$ is that the lift coefficient $\overline{C_{l,y}}$ becomes independent of Re.

By incorporating Re and Ω, we have developed an empirical correlation to predict $\overline{C_{l,y}}$ through multivariable regression analysis:

$$\overline{C_{l,y}} = 0.53 + Re^{-0.11}(2.02\Omega - 0.8)\exp(-0.017\Omega^{1.08}Re^{0.86}). \tag{4.1}$$

Figure 11(a) shows that this correlation effectively captures the numerical results of $\overline{C_{l,y}}$ across the considered range of $40 \leqslant Re \leqslant 200$ and $0.02 \leqslant \Omega \leqslant 1$. The high determination coefficient, $R^2 = 0.9989$, underscores the accuracy of the prediction. Furthermore, the model predicts that $\overline{C_{l,y}}$ becomes independent of Re at $\Omega \approxeq 0.4$, where all curves converge to $\overline{C_{l,y}} \approxeq 0.53$, indicating a common point of overlap.

At higher flow inertia, the lift coefficient exhibits a different behaviour with increasing Re, potentially due to a bifurcation in the base flow regardless of rotation (Citro *et al.* 2016). The increased inertia brings flow instability to the near-wake region accompanied by pronounced pressure fluctuations. We present the evolution of $\overline{C_{l,y}}$ for $Re \geqslant 250$ in figure 11(b). A key distinction is that for $\Omega \leqslant 0.1$, an increase in Re leads to lower values of $\overline{C_{l,y}}$. This effect becomes particularly pronounced as planar symmetry breaks down in the CS regime. For $\Omega \geqslant 0.2$, increasing Re continues to reduce $\overline{C_{l,y}}$, following a mechanism similar to that observed for $Re \leqslant 200$. The common point of overlap of $\overline{C_{l,y}}$ at $Re \geqslant 250$ shifts to a value lower than $\Omega = 0.4$ observed at $40 \leqslant Re \leqslant 200$, and a similar region emerges between $\Omega = 0.2$ and $\Omega = 0.3$, where the variation of $\overline{C_{l,y}}$ with Re is small. It is noteworthy that this region aligns closely with the onset of the KH regime, as shown in figure 4. When the wake flow transitions from the HS regime to the VS and KH regimes, the surface vortex structures generated on the rotating cube tend to stabilise. In this scenario, the increase in flow inertia affects both the upper and lower sides of the cube equally. This similar value of $\overline{C_{l,y}}$ suggests that the pressure difference is maintained at a constant level despite changes in flow inertia.

4.4.2. *Drag coefficient and lift-to-drag ratio*

Along the streamwise direction, we present the evolution of the time-averaged drag coefficient, $\overline{C_d}$, and its relationship with $\overline{C_{l,y}}$ in figure 12. The numerical results indicate that increasing Ω consistently leads to higher values of $\overline{C_d}$ in figure 12(a). This occurs because the rotation reduces the magnitude of the negative pressure in the wake region and shifts it downward, while having minimal impact on the positive pressure on the front surface of the cube, resulting in the increased pressure difference. Same as the flow past a fixed cube, increasing flow inertia has the opposite effect, reducing $\overline{C_d}$ for all the Ω investigated. At $Re \geqslant 250$, we observe a region of insensitivity in $\overline{C_d}$ at $\Omega = 0.2$,

https://doi.org/10.1017/jfm.2025.10292 Published online by Cambridge University Press

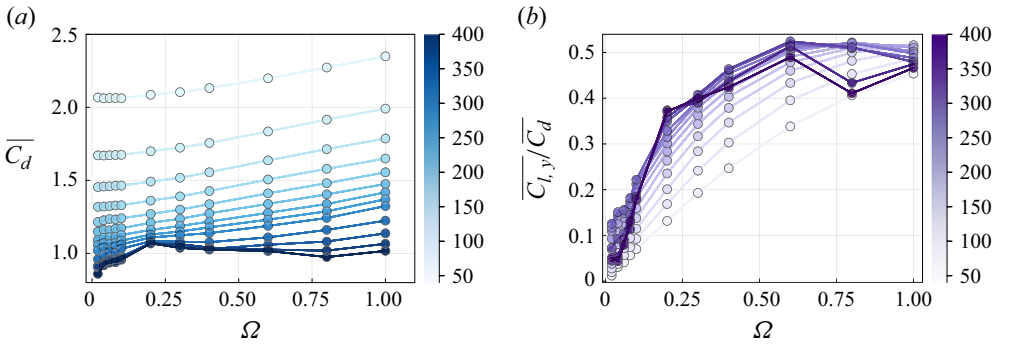

Figure 12. (*a*) Evolution of the time-averaged drag coefficient $\overline{C_d}$ of the rotating RCF4 cube as a function of Ω at $40 \leqslant Re \leqslant 400$. The increasing darkness of the circles represents higher flow inertia. (*b*) Evolution of the lift-to-drag ratio, $\overline{C_{l,y}}/\overline{C_d}$, as a function of Ω at $40 \leqslant Re \leqslant 400$. The increasing darkness of the circles represents higher Re.

where $\overline{C_d}$ remains independent of further increases in Re. One possible explanation is that the shedding frequency of the surface-generated vortices reaches its peak at this specific rotation rate. The rapid release of low-pressure vortex cores raises the time-averaged pressure in the wake region behind the rotating cube. This mechanism is further supported by the evolution of the recirculation region volume V_r, where a local minimum is observed at $\Omega = 0.2$ due to high shedding frequency, as discussed in Appendix D. This high shedding frequency helps sustain the pressure difference between the front and rear faces of the cube, keeping $\overline{C_d}$ at a nearly constant level despite increases in flow inertia from $Re = 250$ to 400. Interestingly, double-hairpin vortex shedding (DHS) is observed in this region at $Re = 250$ and $Re = 300$, as shown in figure 10. To fully leverage our numerical dataset, we derived a novel empirical correlation for $\overline{C_d}$ in (E1) that builds upon the classical Schiller–Naumann formulation (Schiller & Naumann 1935). The derivation and resulting expression are detailed in Appendix E.

Knowing the behaviour of both $\overline{C_{l,y}}$ and $\overline{C_d}$, we now plot the ratio of these two coefficients, $\overline{C_{l,y}}/\overline{C_d}$, in figure 12(*b*) to gain further insights into the hydrodynamic forces. A general trend is that the ratio $\overline{C_{l,y}}/\overline{C_d}$ increases with Ω. The effects of flow inertia tend to increase the ratio $\overline{C_{l,y}}/\overline{C_d}$, particularly for $Re \leqslant 200$. However, at $Re \geqslant 250$, the flow inertia has the opposite effect, decreasing this ratio. We know that the flow inertia and the particle rotation are competing factors in vortex generation. For $Re \geqslant 250$, the increasing flow inertia strengthens the vortex pairs on both the upper and lower surfaces of the rotating cube. This enhanced vortex activity moderates the strong lift forces generated by the Magnus effect, preventing further amplification of Magnus-induced lift and stabilising $\overline{C_{l,y}}/\overline{C_d}$. The moderating effect of Re on the ratio is particularly pronounced in both slow rotation ($0.02 \leftarrow \Omega$) and fast rotation cases ($\Omega \rightarrow 1$). One exception is the region of drag insensitivity at $\Omega = 0.2$ for $250 \leqslant Re \leqslant 400$, where we see the $\overline{C_{l,y}}/\overline{C_d}$ keeps increasing with Re. It is important to highlight that in all the cases investigated, $\overline{C_{l,y}}/\overline{C_d}$ remains consistently bounded below 0.6, as depicted in figure 12(*b*). With increasing Ω, $\overline{C_{l,y}}/\overline{C_d}$ does not increase monotonically, but instead reaches a plateau, as the flow dynamics at high rotation rates restrain further amplification of lift relative to drag.

4.4.3. *Rotation coefficient*

Given the significant impact of Ω and Re on the Magnus effect, we calculate the rotation coefficient, using (2.8), to quantify how effectively the rotation rate contributes

https://doi.org/10.1017/jfm.2025.10292 Published online by Cambridge University Press

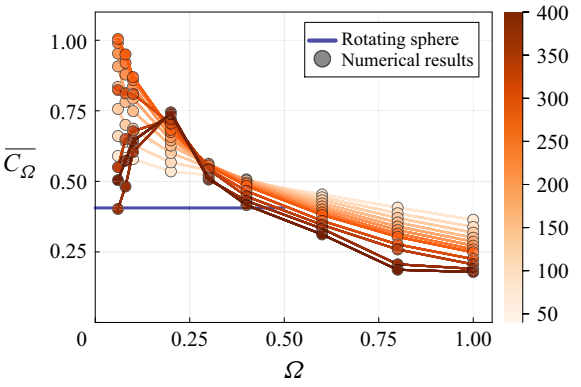

Figure 13. Evolution of the time-averaged rotation coefficient $\overline{C_\Omega}$ of the rotating RCF4 cube as a function of $0.06 \leqslant \Omega \leqslant 1$ at $40 \leqslant Re \leqslant 400$. The increasing darkness of the circles represents higher Re. The rotation coefficient of a rotating sphere, $C_{\Omega,S} = 0.41$, is marked by a blue horizontal line for $\Omega \leqslant 0.5$, as reported by Clanet (2015), providing a comparative reference.

to generating lift. A higher $\overline{C_\Omega}$ indicates a greater efficiency of Magnus effect for a given Ω. In figure 13, we show the evolution of the time-averaged rotation coefficient $\overline{C_\Omega}$ as a function of Ω, with marker darkness increasing with Re.

We observe that the efficiency of lift generation via the Magnus effect decreases monotonically with increasing Ω for low flow inertia cases $Re \leqslant 200$. For example, at $Re = 40$, $\overline{C_\Omega}$ drops from 0.55 at $\Omega = 0.06$ to 0.4 at $\Omega = 1$, indicating that the flow becomes less responsive to rotation. The effects of increasing Re on $\overline{C_\Omega}$ are twofold. For $\Omega \leqslant 0.2$, higher flow inertia enhances the interaction between the rotating cube and the fluid, strengthening the Magnus effect. However, for faster-rotating cubes at $\Omega \geqslant 0.3$, increasing Re reduces $\overline{C_\Omega}$, as the enhanced flow unsteadiness decreases the pressure difference between the top and bottom of the particle, diminishing lift generation. As shown in figure 11, the decline in $\overline{C_{l,y}}$ with Re at $\Omega \geqslant 0.4$ is a direct result of the diminished efficiency of the Magnus effect. At higher flow inertia, $Re \geqslant 250$, $\overline{C_\Omega}$ generally decreases, except at $\Omega = 0.2$. At low rotation rates, $\Omega \leqslant 0.1$, increasing Re reduces lift due to chaotic shedding, which disrupts vortex distribution and diminishes the lift force. However, at $\Omega = 0.2$, $\overline{C_\Omega}$ shows a distinct trend, continuing to increase across the entire Reynolds number range $40 \leqslant Re \leqslant 400$, indicating enhanced rotational efficiency. This behaviour is closely linked to the reorganisation of vortex pairs and their high shedding frequency at $\Omega = 0.2$. A comparison is made with the characteristic rotation coefficient of a sphere $C_{\Omega,S} = 0.41$ for $\Omega \leqslant 0.5$ (Clanet 2015). The blue horizontal line in figure 13 serves as a reference to compare the rotating cube with a sphere under similar conditions. The cube demonstrates higher rotational efficiency, particularly at lower rotation rates, indicating a stronger Magnus effect due to its sharp edges. Analogous to the empirical correlation for $\overline{C_{l,y}}$, we propose an equally valuable correlation for $\overline{C_\Omega}$ at $40 \leqslant Re \leqslant 200$ in (E2) (see Appendix E).

From a broader perspective, the force coefficients ($\overline{C_d}$, $\overline{C_{l,y}}$ and $\overline{C_\Omega}$) of the RCF4 provide essential insights on trajectories of settling angular particles. In our prior work (Gai & Wachs 2024), we demonstrated that the Magnus force and hydrodynamic torque play significant roles in shaping the trajectory of a freely settling cube, sustaining an intriguing helical motion in the HS regime. The Magnus force serves as the primary driver of the cube horizontal motion. Then, the resulting rotation-induced drift generates

https://doi.org/10.1017/jfm.2025.10292 Published online by Cambridge University Press

a secondary Magnus force that amplifies the settling drag. It is also demonstrated that the enhanced hydrodynamic torque triggers the transition from the oblique to the helical settling regimes. An additional analysis of the hydrodynamic torque $\overline{T_z}$ is presented in Appendix F, where we propose a simple scaling law to model $\overline{T_z}$ of the RCF4 over the range $200 \leqslant Re \leqslant 400$, yielding a correlation with an $r^2 = 0.999$.

In previous studies, the absence of accurate correlations necessitated the use of approximate values in force balance analysis to gain insight into the underlying physics. By providing more accurate lift, drag and torque coefficients, and correlations for a centre-fixed rotating cube, we offer an approach to overcome this limitation, paving the way for more robust and physically grounded analyses in future research.

4.5. *Vortex shedding frequency*

While time-averaged drag and lift forces serve as essential design and engineering metrics, understanding the unsteady fluctuations and their frequencies is crucial for analysing particle trajectory instabilities, mixing and collision dynamics. Figures 8–10 reveal that the flow past a rotating cube displays a variety of vortex shedding patterns. The shedding frequency increases with rising Ω, before stabilising in the VS and KH regimes. To clarify how the vortex shedding frequencies evolve with Ω, we apply fast Fourier transform (FFT) to the temporal evolution of the lift force, resulting in the frequency spectra presented in figure 14. Three Reynolds numbers ($Re = 80$, 160 and 400) are selected as representative examples of low, moderate and high flow inertia. Each subpanel shows the frequency spectrum (solid blue lines) from $\Omega = 0.02$ to $\Omega = 1$, with the frequency of the primary peak annotated next to it. We report in each subpanel the rotation rate Ω as a red dashed line in addition to reporting its value in the top right corner. As reference points, we also plot two characteristic frequencies of the flow past a fixed cube: (i) the vortex shedding frequency, i.e. the primary peak, as yellow dashed lines and (ii) the first harmonic of the primary peak as grey dashed lines (Gai & Wachs 2023*b*).

At $Re = 80$, the frequency spectrum shows a single dominant peak across all rotation rates $0.02 \leqslant \Omega \leqslant 1$, with values increasing proportionally to Ω. As shown in figure 23, at low flow inertia, the wake vortical structures using $\lambda_2 = -1$ remain steady or fragmented within the SV, UV and VS regimes. Vortex shedding occurs only at $\Omega = 0.1$ and $\Omega = 0.2$ in the HS regime at $Re = 80$. The dominant frequency seen in the blue curves in figure 14(*a*) corresponds to the generation and shedding of the upper and lower streamwise vortex pairs, as illustrated in figure 9. The lower panel of figure 9 shows that each effective face of the rotating cube produces one pair of upper vortices and one pair of lower vortices. Consequently, for a rotating cube with a four-fold axis, four pairs of upper/lower streamwise vortices are generated during a complete rotation cycle. At higher flow inertia, $Re = 160$, the primary peak values in figure 14(*b*) remain nearly identical to those at $Re = 80$, despite differences in the flow regime transition sequence. For $\Omega \geqslant 0.3$, a small secondary peak emerges as the first harmonic frequency, likely due to nonlinear effects such as intricate vortex interactions or flow instabilities. At $Re = 400$, while the primary peak is still similar to those at lower Reynolds numbers, the first harmonic becomes significantly more pronounced. Interestingly, a distinct high-intensity region appears near the characteristic vortex shedding frequency for a fixed cube, $\mathcal{S}tr_0 = 0.11$. Between $\Omega = 0.3$ and $\Omega = 0.8$, the high-value plateau around $\mathcal{S}tr_0 = 0.11$ stands out, reflecting the persistent obstacle effect of the cube in the flow, independent of its rotation.

To capture the overall behaviour of the shedding frequency, we apply FFT to all cases investigated and compute $\mathcal{S}tr$ using (2.9). The results are plotted as a function of Ω in

https://doi.org/10.1017/jfm.2025.10292 Published online by Cambridge University Press

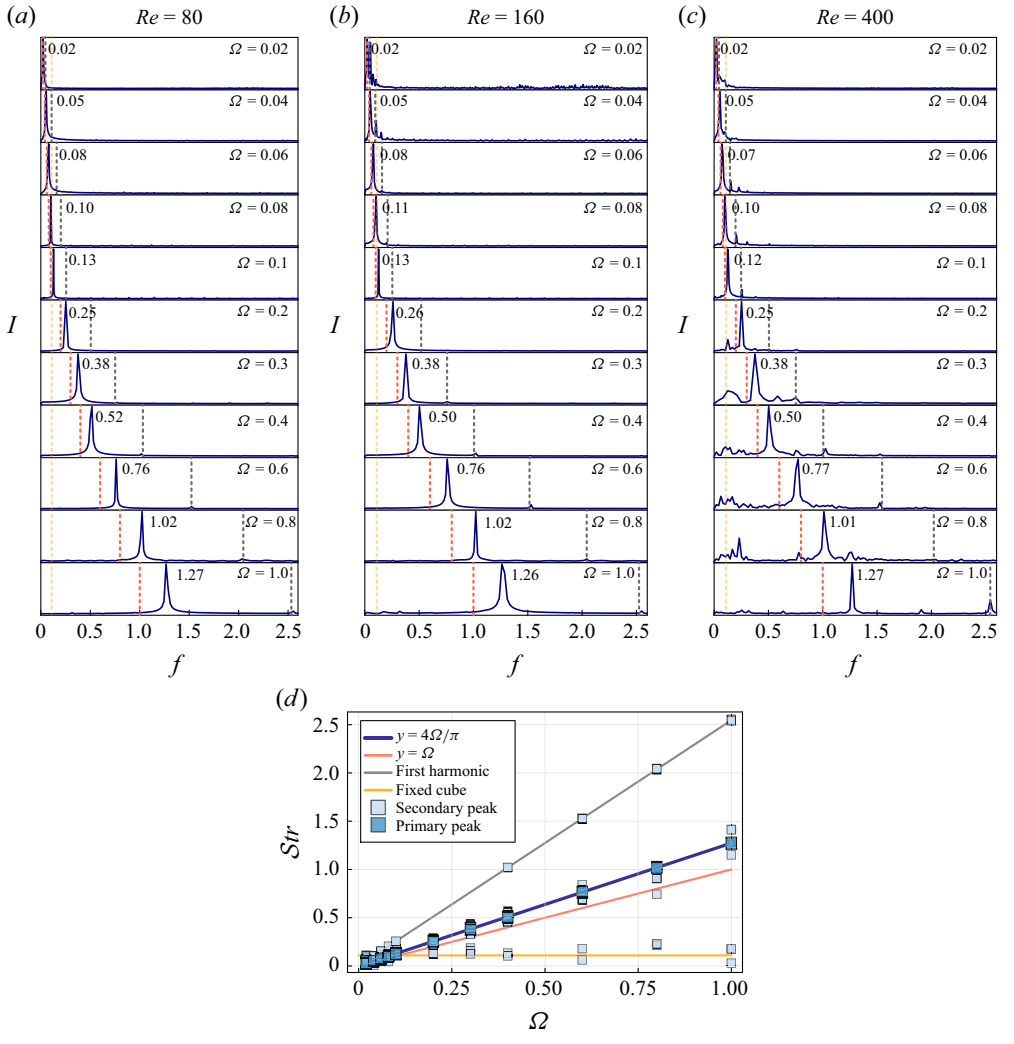

Figure 14. (*a–c*) Vortex shedding frequency f spectrum of the rotating RCF4 cube at $Re = 80$, 160 and 400. I represents the frequency intensity obtained via FFT and is displayed on a linear scale in each panel. (*d*) Strouhal number $\mathcal{S}tr$ of the primary and secondary peaks as a function of Ω for all values of Ω and Re considered. The blue curve represents the fitting for the primary peak $\mathcal{S}tr_1$, following $y = 4\Omega/\pi$, while the red curve shows the imposed rotation rate, $y = \Omega$. The grey curve indicates the first harmonic of the primary peak frequency, and the yellow curve corresponds to the characteristic $\mathcal{S}tr_0 = 0.11$ of the flow past a fixed cube (Gai & Wachs 2023*b*). Dashed lines in the corresponding colours are reported in panel (*a–c*) in each case.

figure 14(*d*). The dark and light blue square markers represent the Strouhal numbers based on the primary peak ($\mathcal{S}tr_1$) and the secondary peak ($\mathcal{S}tr_2$), respectively. By applying linear regression to the evolution of $\mathcal{S}tr_1$ with Ω, we derive the following relationship:

$$\mathcal{S}tr_1 = \frac{4}{\pi}\Omega \tag{4.2}$$

with a coefficient of determination $R^2 = 0.99$. The fitting curve is represented by the navy solid line in figure 14(*d*). This equation describes the shedding frequency of the

https://doi.org/10.1017/jfm.2025.10292 Published online by Cambridge University Press

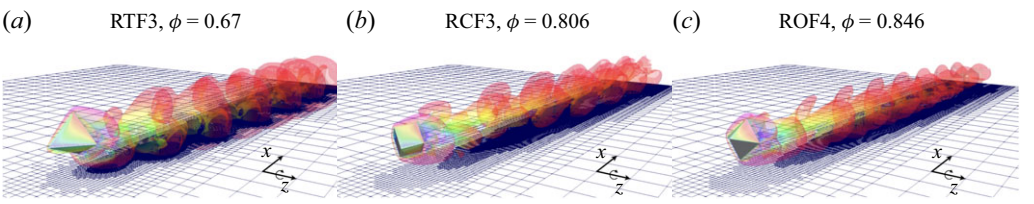

Figure 15. Configuration of the flow past a transversely rotating angular particle at $Re = 100$ and $\Omega = 0.2$ with rotation axis along the z-direction, illustrating wake vortex structures identified by $\lambda_2 = -1$, coloured by the streamwise velocity u_x (red for high velocity and blue for low velocity). (*a*) Rotating RTF3 tetrahedron with a three-fold axis, (*b*) rotating RCF3 cube with a three-fold axis and (*c*) rotating ROF4 octahedron with a four-fold axis.

streamwise vortex pairs on the particle surface, and is therefore closely correlated with both the rotation rate Ω and the rotational symmetry fold ($n_\Omega = 4$ for RCF4).

In figure 14(*d*), the secondary peaks $\mathcal{S}tr_2$ from all 143 simulations of RCF4 can be clearly categorised into three distinct groups: (i) those adjacent to the primary peak, representing the shedding of vortex pairs from the cube surface; (ii) those along the curve of the first harmonics (grey solid line), reflecting more intricate vortex interactions; and (iii) those near the fixed cube frequency $\mathcal{S}tr_0 = 0.11$ (orange horizontal line), which corresponds to the obstacle effect of the cube without rotation. In general, increasing flow inertia amplifies the intensity of the first harmonics. For flows with low inertia, $Re \leqslant 200$, the wake structure shedding frequency, identified using the $\lambda = -1$ criterion, is primarily dominated by $\mathcal{S}tr_1$ for $\Omega \leqslant 0.2$, as shown in figure 8(*a*). In the KH regime, the shedding of wake vortices caused by K-H instabilities occurs farther from the rear surface of the particle, making them difficult to observe directly in figure 14. At higher flow inertia, as seen in figure 10, the obstacle effect of the cube becomes dominant in the CS regime. Their wake structure shedding frequency is predominantly governed by $\mathcal{S}tr_2 \approx 0.11$, closely aligned with the orange curve in figure 14(*d*). Additional vortex shedding patterns are presented in Appendix C for further reference.

5. Extending insights to general angular particles

In this section, we extend our analysis from the cube to other rotating angular particles to further investigate the impact of particle shape on the Magnus effect and wake instability. A key challenge in studying angular particles is the infinite number of possible angular positions, particularly when the particle is rotating. To address this, we focus on the rotation axis of the particle and explore how the number of rotational symmetry folds n_Ω affects the vortex shedding and its suppression, offering insights into the relationship between particle geometry and wake instability.

In addition to the four-fold rotating cube (RCF4) discussed earlier, we examine three angular particles: a tetrahedron (three-fold, RTF3), another cube (three-fold, RCF3) and an octahedron (four-fold, ROF4), with their rotation axis illustrated in figure 2. We recall that n_Ω refers to the number of times an angular particle can be rotated by equal angles around the axis while retaining an identical appearance. To provide a clearer visualisation of their rotation in the computational domain, figure 15 presents the flow configurations in the three additional cases. At the same Re and Ω, the wake structures vary significantly depending on both the particle angularity ϕ and n_Ω. We perform 99 additional numerical simulations of the flow past these three angular particles, covering $Re = 60$, 100 and 160, and a range of $0.02 \leqslant \Omega \leqslant 1$.

https://doi.org/10.1017/jfm.2025.10292 Published online by Cambridge University Press

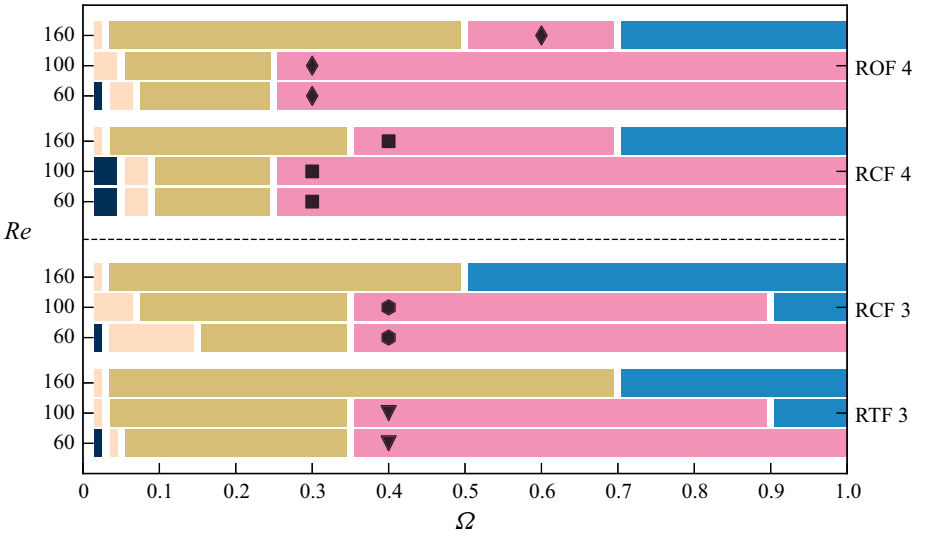

Figure 16. Regime transitions of the flow past a rotating angular particle at $Re = 60$, 100 and 160 for $0.02 \leqslant \Omega \leqslant 1$. Onset of vortex suppression for RTF3 (▲), RCF3 (⬢), RCF4 (■) and ROF4 (⧫).

5.1. *Influence of the number of rotational symmetry folds on flow regimes and wake instability*

For a comprehensive view of the effects of particle shape and n_Ω on flow regime transitions, we present the regime map for flows past transversely rotating angular particles at $60 \leqslant Re \leqslant 160$ in figure 16. The lower subpanel compares the two angular particles with $n_\Omega = 3$, specifically RCF3 and RTF3, while the upper subpanel focuses on the particles with $n_\Omega = 4$. The regimes of the RCF4 are included for comparison with the ROF4. For consistency, the same colour scheme as that used in the regime map in figure 4 is used. Within the selected range of Re, figure 16 illustrates the transition sequence, starting from the SV regime to vortex shedding in the HS regime, followed by vortex suppression in the VS and KH regimes.

A key observation from figure 16 is that n_Ω plays a dominant role in regime transitions. For the three-fold cases, RTF3 and RCF3 exhibit highly similar transition sequences, as shown in the lower subpanel. Vortex suppression begins at the same rotation rate, $\Omega = 0.4$, for both $Re = 60$ and 100. The KH regime replaces the VS regime at $Re = 160$ in both cases. In the four-fold cases, vortex suppression occurs at a lower rotation rate, $\Omega = 0.3$, for both RCF4 and ROF4 at $Re = 60$ and 100. A slight difference emerges at $Re = 160$, where vortex suppression for ROF4 occurs at a higher Ω compared with RCF4. Overall, the regime transition for RCF4 shows strong similarities with the regime transition for ROF4.

By comparing the upper and lower subpanels, we observe that increasing n_Ω leads to vortex suppression at a lower critical Ω. Within the range of Re discussed, particle rotation stabilises the wake structure through vortex merging, while flow inertia tends to induce instabilities. A higher n_Ω enhances this stabilising effect, as seen in the four-fold cases where the VS regime persists at $Re = 160$. By contrast, in the three-fold cases, the VS regime is replaced by the KH regime at the same Re, as shown in the lower subpanel. Particle angularity ϕ has less impact than n_Ω on regime transitions. As illustrated in figure 16, RTF3 ($\phi = 0.67$) begins vortex shedding at a lower rotation rate than the less angular RCF3 ($\phi = 0.806$). However, this trend does not hold for the four-fold cases, as RCF4 ($\phi = 0.806$) and ROF4 ($\phi = 0.846$) exhibit the opposite behaviour.

https://doi.org/10.1017/jfm.2025.10292 Published online by Cambridge University Press

To elucidate the effects of ϕ and n_Ω on wake instabilities, figure 17 illustrates the wake structures for flows at $Re = 100$ with rotation rates in the range $0.1 \leqslant \Omega \leqslant 0.4$. We show a side view of the wake vortical structures for the three-fold angular particles RTF3 and RCF3 in figure 17(*a*). At $\Omega = 0.1$, RCF3 exhibits more fragmented vortex structures than RTF3, due to the higher number of effective faces $N_\mathcal{F}$. In the flow configuration of figure 15(*b*), the three-fold cube RCF3 has six faces $N_\mathcal{F} = 6$ contributing to vortex generation during rotation, while the three-fold tetrahedron RTF3 has only three $N_\mathcal{F} = 3$, as its fourth face is parallel to the flow and hardly impacts the wake. At $\Omega \geqslant 0.2$, the wake structures and shedding frequencies of RTF3 and RCF3 become more similar. Although some shape effects remain noticeable at $\Omega = 0.2$, they diminish at $\Omega = 0.3$, and by $\Omega = 0.4$, both RTF3 and RCF3 exhibit the same steady wake structures in the VS regime. In figure 17(*b*), the wake structures behind RCF4 and ROF4 exhibit a striking similarity in both topology and frequency, with minimal influence from angularity. Note that ROF4 features two faces per fold; however, since they are in phase, they operate as one single effective face per fold. Hence, ROF4 and RCF4 both have four effective faces per rotation period $N_\mathcal{F} = 4$. At $\Omega = 0.3$, both particles exhibit clear signs of vortex suppression. Despite differences in shape and angularity, RCF4 and ROF4 behave almost identically, suggesting that n_Ω is the key factor that controls wake dynamics.

We further plot the isosurfaces of streamwise vortices $\omega_x = \pm 0.03$ in figure 17(*c*) to compare RTF3 and RCF3. The vortex generation on the surface of the tetrahedron differs significantly from that on the surface of the cube. In the RTF3 case at $\Omega = 0.1$, an entwined structure of blue and red vortices is observed, while in the RCF3 case, the two opposite-signed vortices are more separated, positioned on either side of the horizontal centreline in the x-z plane. This difference in vortex pair generation explains the variation in wake structures between RTF3 and RCF3. From $\Omega = 0.3$ to $\Omega = 0.4$, we highlight the merging of three blue streamwise vortices into a single one, as indicated by the yellow arrow. The distribution of ω_x in the y-z plane in the particle wake shows that planar symmetry is already broken in these cases. However, by $\Omega = 0.4$, the wake structure becomes steady as a result of vortex merging. Despite differences in vortex patterns between RTF3 and RCF3, the merging process remains consistent in both cases.

Similarly, figure 17(*d*) presents the isosurface of $\omega_x = \pm 0.03$ for RCF4 and ROF4. The distribution of ω_x in the y-z plane at $x = x_p + 1.5$ is shown in the middle of the figure, with green lines indicating their position in the x-z plane. Since RCF4 and ROF4 both have four effective faces during rotation, we observe highly symmetric vortex pairs in both the x-z and y-z planes. For $0.2 \leqslant \Omega \leqslant 0.3$, the yellow arrow highlights the merging of three smaller blue vortices into a long blue tail in the ROF4 case. This indicates that vortex suppression occurs due to the merging of vortices of same sign, a process enhanced by the increased rotation rate. Remarkably, this mechanism, thoroughly discussed in § 4.3.1 for RCF4, remains consistent and universal across all particle shapes and number of rotational symmetry folds.

5.2. *Impact of particle angularity on hydrodynamic forces*

We now shift our attention from the wake structure to the rotating particle itself, examining how ϕ and n_Ω affect the hydrodynamic forces acting on the particle. Figure 18 illustrates the evolution of $\overline{C_{l,y}}$ of the three angular particles – RTF3, RCF3 and ROF4 – as a function of increasing Ω at $Re = 60$–160. It is clear that $\overline{C_{l,y}}$ increases monotonically with Ω at any given Re. At $Re = 60$, particle angularity has a pronounced effect, significantly amplifying the lift. The rotating tetrahedron RTF3 in figure 18(*a*) reaches $\overline{C_{l,y}} = 1.12$, which is 15 % higher than RCF3 in figure 18(*b*) and 20 % higher than ROF4 in figure 18(*c*). As flow

https://doi.org/10.1017/jfm.2025.10292 Published online by Cambridge University Press

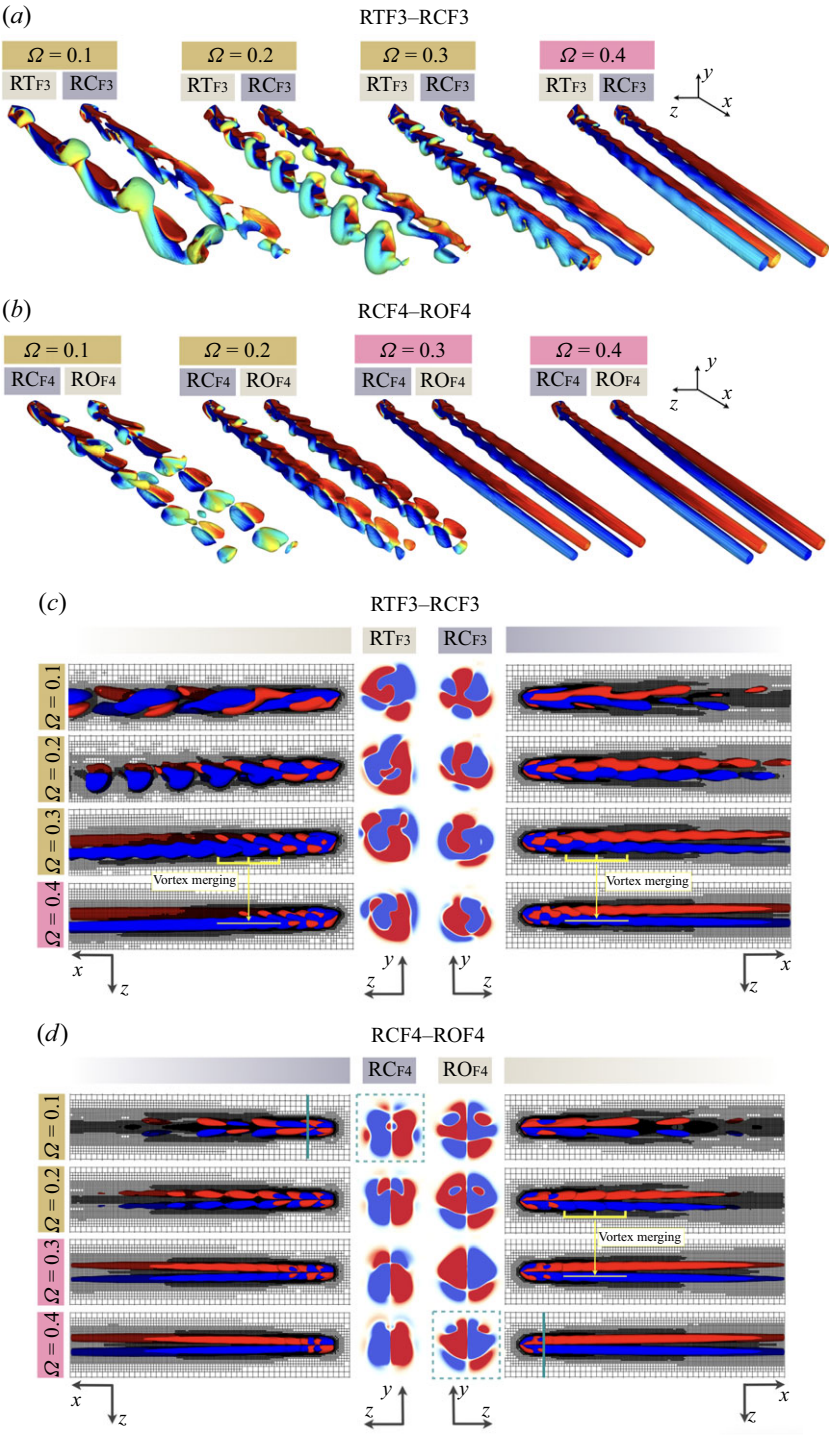

Figure 17. Evolution of wake structures before and after the vortex suppression in the flow past a rotating angular particle at $Re = 100$. Side view of the wake structures, identified by $\lambda_2 = -1$ and coloured by u_x, are shown for comparison between the (*a*) three-fold cases and (*b*) four-fold cases. Top views of the wake structures, identified by vorticity $\omega_x = \pm 0.03$ in the x-z plane, are compared for the (*c*) three-fold cases and (*d*) four-fold cases. The ω_x distribution in the y-z plane at $x = x_p + 1.5$ are also depicted in panels (*c*) and (*d*).

https://doi.org/10.1017/jfm.2025.10292 Published online by Cambridge University Press

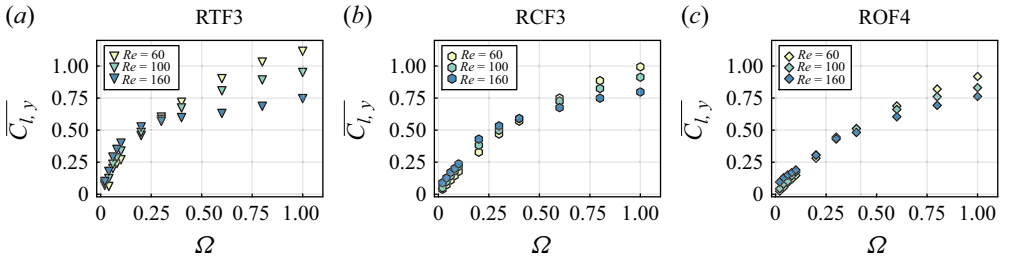

Figure 18. Evolution of $\overline{C_{l,y}}$ of a rotating angular particle as a function of Ω at $Re = 60$, 100 and 160: (*a*) RTF3; (*b*) RCF3 and (*c*) ROF4.

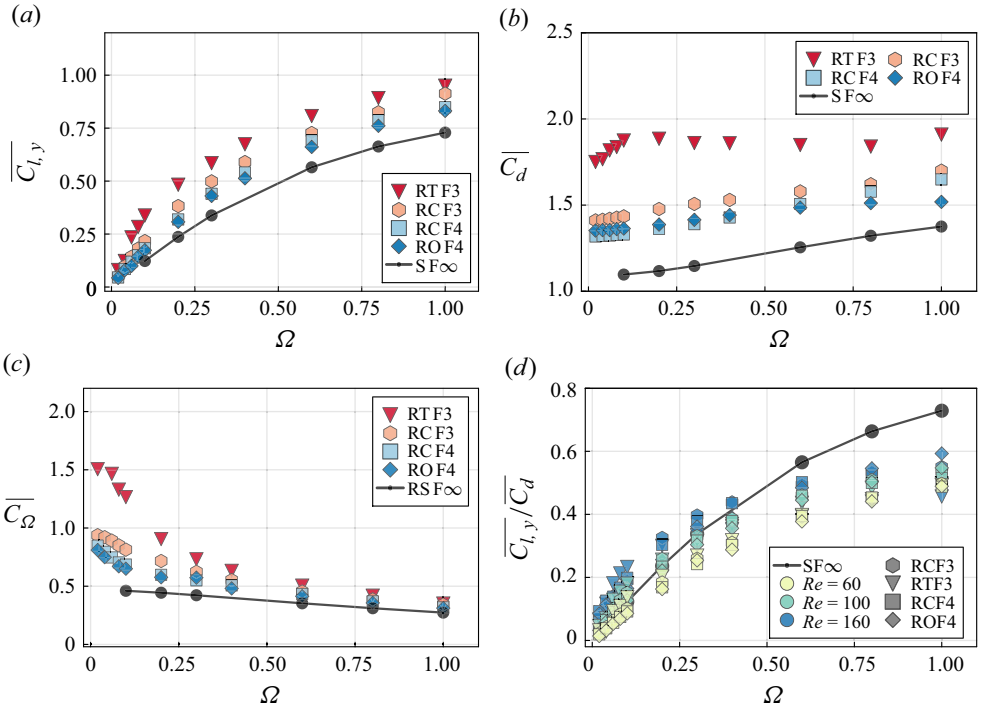

Figure 19. Effects of particle angularity on the hydrodynamic forces exerted on a rotating angular particle: (*a*) lift coefficient $\overline{C_{l,y}}$ at $Re = 100$; (*b*) drag coefficient $\overline{C_d}$ at $Re = 100$; (*c*) rotation coefficient $\overline{C_\Omega}$ at $Re = 100$ and (*d*) the lift-to-drag ratio $\overline{C_{l,y}}/\overline{C_d}$ at $Re = 60$–160. The case of the flow past a rotating $RSF\infty$ sphere at $Re = 100$ is provided as a reference and shown by the black solid lines.

inertia increases, $\overline{C_{l,y}}$ tends to decrease. By $Re = 160$, the influence of particle angularity diminishes, especially at higher rotation rates. For instance, at $\Omega = 1$, all three angular particles exhibit the same lift coefficient $\overline{C_{l,y}} = 0.75$.

Recognising that particle shape has a more pronounced impact in low-inertia flows, we fix $Re = 100$ and examine the evolution of the lift, drag and rotation coefficients in figure 19 to gain deeper insights into the hydrodynamic behaviour. Figure 19(*a*) illustrates the evolution of $\overline{C_{l,y}}$ as a function of Ω for all the shapes examined in this study. It is clear that particle angularity enhances the Magnus effect, leading to higher $\overline{C_{l,y}}$. Particles with a three-fold symmetry axis generate higher lift compared with those with a four-fold symmetry axis, and both significantly outperform the sphere, which represents the infinite-fold symmetry case (RSF∞). Additionally, $\overline{C_d}$ is affected by ϕ, with the tetrahedron

https://doi.org/10.1017/jfm.2025.10292 Published online by Cambridge University Press

showing significantly higher values than the other shapes, as seen in figure 19(*b*). This behaviour results from the large recirculation region volume V_r in the RTF3 case, as depicted in figure 24(*e*) in Appendix D. Here, $\overline{C_d}$ of RTF3 increases until $\Omega = 0.1$, after which it stabilises around 1.9 and remains constant up to $\Omega = 1$. Meanwhile, RCF3 exhibits slightly higher drag values than RCF4 and ROF4. All angular particles exhibit higher $\overline{C_d}$ than the rotating sphere.

The $\overline{C_\Omega}$ increases when particle angularity increases, as shown in figure 19(*c*), demonstrating that sharp edges enhance the efficiency of the Magnus effect. It is especially pronounced in slow-rotating cases $\Omega \leqslant 0.6$. For example, at $\Omega = 0.1$, RTF3 exhibits a $\overline{C_\Omega}$ two and a half times greater than that of the sphere. However, as the rotation rate increases, the influence of particle angularity diminishes and $\overline{C_\Omega}$ in all cases converges to a similar value of 0.35 at $\Omega = 1$, where particle shape no longer plays a significant role. Figure 19(*d*) illustrates the evolution of the ratio $\overline{C_{l,y}}/\overline{C_d}$ for particles of various shapes at $Re = 60$–160. Unlike the individual lift and drag coefficients, $\overline{C_{l,y}}/\overline{C_d}$ shows very limited dependence on particle angularity. In contrast, flow inertia plays a more noticeable role, contributing to the increase of the ratio. It is noteworthy that the rotating sphere (plotted in black solid line for $Re = 100$) exhibits values comparable to the angular particles at $\Omega \leqslant 0.4$. However, at $\Omega \geqslant 0.6$, the sphere shows higher values than the angular particles, as indicated by the light green markers. Remarkably, for all particle shapes, the ratio $\overline{C_{l,y}}/\overline{C_d}$ remains consistently bounded by 0.6 across the entire range of $0.02 \leqslant \Omega \leqslant 1$. The upper bound 0.6 also holds true for all $40 \leqslant Re \leqslant 400$ considered in RCF4 cases, as shown in figure 12(*b*). This key finding reveals a consistent upper limit on the lift-to-drag ratio of flow past a rotating angular particle, independent of particle shape and rotation rate. In addition to affecting hydrodynamic forces, increased particle angularity substantially amplifies hydrodynamic torques. Further details on how particle angularity influences $\overline{T_z}$ are provided in Appendix F.

5.3. *Role of effective faces in determining shedding frequency*

From the previous sections, we know that n_Ω significantly influences vortex generation, while ϕ has a greater impact on the hydrodynamic forces. We now shift our focus to the shedding frequency, a crucial aspect of wake dynamics driven by vortex shedding. The key question we aim to address is how n_Ω of different angular particles affects $\mathcal{S}tr$. Similarly to what we did to produce figure 14, we apply FFT to the temporal evolution of $C_{l,y}$ for RTF3, ROF4 and RCF3, and compute the corresponding $\mathcal{S}tr$ values, shown in figure 20.

As discussed in the RCF4 case, each effective face generates a pair of oppositely signed upper/lower streamwise vortices as it pushes fluid into the wake. Since RCF4 has four effective faces, it produces four pairs of upper/lower streamwise vortices per rotation period. Extending this mechanism to other angular particles, we hypothesise that the number of vortex pairs generated per period is proportional to the number of effective faces $N_\mathcal{F}$. In Fourier space, this implies that $\mathcal{S}tr$ associated with the primary peak should be proportional to $N_\mathcal{F}$. Based on this reasoning, we propose the following model for $\mathcal{S}tr_1$, as derived from (4.2):

$$\mathcal{S}tr_1 = \frac{N_\mathcal{F}}{\pi}\Omega. \tag{5.1}$$

We plot the prediction of $\mathcal{S}tr_1$ from (5.1) for the RTF3 case as a function of Ω and compare it with the numerical results in figure 20(*a*). RTF3 has a three-fold rotational symmetry, corresponding to three effective faces $N_\mathcal{F} = 3$. As shown in figure 20(*a*), the numerical data align closely with the prediction from (5.1), with all primary peaks falling

https://doi.org/10.1017/jfm.2025.10292 Published online by Cambridge University Press

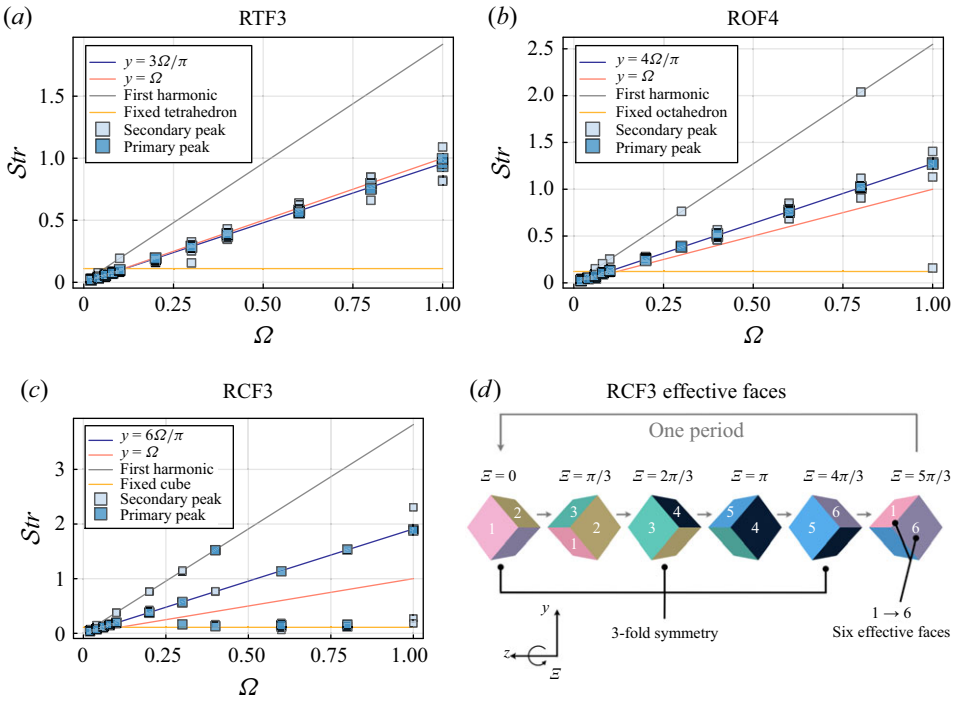

Figure 20. $\mathcal{S}tr$ of the primary and secondary peaks as a function of Ω for (*a*) RTF3, (*b*) ROF4 and (*c*) RCF3. The blue curve represents the proposed model for the primary peak $\mathcal{S}tr_1$, while the red curve corresponds to $y = \Omega$. The grey curve indicates the first harmonic of the primary peak frequency, and the yellow curve denotes the characteristic $\mathcal{S}tr_0$ of the flow past a fixed tetrahedron $\mathcal{S}tr_0 = 0.11$ in panel (a), a fixed octahedron $\mathcal{S}tr_0 = 0.12$ in panel (*b*) and a fixed cube $\mathcal{S}tr_0 = 0.11$ in panel (*c*) (Gai & Wachs 2023*b*). (*d*) Rear view of RCF3 with snapshots showing incremental rotation angles ($\Delta\Xi = \pi/3$) over a complete rotation period, where the six effective faces of RCF3 are depicted in different colours.

along the prediction curve (navy solid line). The secondary peaks also follow the primary peaks closely. Similarly, in the ROF4 case (figure 20*b*), the primary peaks match very well the model prediction, with $N_{\mathcal{F}} = 4$. Several secondary peaks appear along the first harmonic curve, indicating intensified vortex interactions.

RCF3 presents a unique case because, although it has a three-fold rotational symmetry, each fold consists of two effective faces, resulting in a total of six effective faces, compared with only three in the RTF3 case. In figure 20(*d*), we show a rear view of RCF3 with snapshots illustrating incremental rotation angles $\Delta\Xi = \pi/3$ over a complete rotation period around the z-axis. Starting from the initial angular position at $\Xi = 0$, each rotation by $\Delta\Xi = 2\pi/3$ returns the cube to the same angular position, confirming its three-fold rotational symmetry. In figure 20(*d*), the six distinct faces, each highlighted in a different colour, all contribute to pushing fluid into the wake region during a single period, leading to $N_{\mathcal{F}} = 6$. As a result, the frequency distribution in figure 20(*c*) shows distinct behaviour compared with figure 20(*a*). While most of the primary peaks align well with the prediction of (5.1), several primary peaks correspond to $\mathcal{S}tr_0$, i.e. to the Strouhal number of the flow past a fixed cube. This occurs because, at higher shedding frequencies (with six pairs of vortices per period), the streamwise upper vortex pairs generated by each effective face become relatively weak, allowing the build-up and release process of the recirculation region in the lower wake to dominate. Additionally, more secondary peaks appear along the first harmonic curve.

https://doi.org/10.1017/jfm.2025.10292 Published online by Cambridge University Press

Although $N_{\mathcal{F}}$ directly influences $\mathcal{S}tr_1$, the vortex suppression is noted to be primarily governed by n_{Ω}. Recall that in cases of low flow inertia, vortex suppression occurs at $\Omega = 0.3$ for RCF4 and ROF4, and at $\Omega = 0.4$ for RTF3 and RCF3. An intriguing observation is that multiplying these critical rotation rates by the corresponding number of rotational symmetry folds yields a critical Strouhal number, $\mathcal{S}tr_c = n_{\Omega}\Omega_c/\pi \approx 0.38$, which is nearly four times the characteristic Strouhal number of the flow past a fixed angular particle, $\mathcal{S}tr_0 \approx 0.1$. This suggests that the shedding frequency of streamwise vortex pairs driven by the effective faces must be sufficiently high to promote vortex merging, eventually leading to suppression. For angular particles, this process can be more easily controlled, as the finite number of effective faces allows for fine-tuning of the shedding frequency to stabilise the wake.

6. Conclusions

We explored the dynamics, wake instabilities and regime transitions of inertial flow past transversely rotating angular particles. Our findings provide new insights into how particle angularity and rotational symmetry fold influence flow instabilities, deepening our understanding of how sharp edges affect inertial flow.

By investigating the rotating cube (RCF4, four-fold cube), we find the driving mechanisms of vortex generation on the front inclined faces, and the merging process on the cube surface and in the wake region. Our results reveal intricate vortex shedding structures, and show that the generation and merging of streamwise vortex pairs are key mechanisms leading to vortex suppression. The four effective faces of RCF4 produce four pairs of opposite-signed upper/lower streamwise vortices per rotation period. At low rotation rates, $\Omega \leqslant 0.2$, rotation induces periodic impulses to the wake, resulting in periodic hairpin vortex shedding at lower Re compared with a fixed cube. However, as the rotation rate increases to $\Omega = 0.3$, the higher shedding frequency of streamwise vortex pairs promotes the merging of vortices with the same sign, leading to vortex suppression and wake stabilisation. At even higher rotation rates, the stabilised wake becomes wavy further downstream due to the onset of Kelvin–Helmholtz instabilities, similar to the rotating sphere.

A detailed analysis of the hydrodynamic forces, with a focus on the Magnus effect, reveals how the sharp edges of the particle significantly influence the lift, drag, rotation coefficients and the shedding frequency. In low-inertia flows, $Re \leqslant 200$, an intriguing fixed point is observed in the evolution of $\overline{C_{l,y}}$. At $\Omega = 0.4$, the Magnus effect becomes largely independent of flow inertia, with $\overline{C_{l,y}}$ stabilising at a constant value of 0.5, regardless of Re. The evolution of drag and rotation coefficients also exhibits unique behaviours due to the sharp edges of the cube. The spectrum of shedding frequency of RCF4 shows that the primary peak in the frequency spectrum is directly linked to the shedding of streamwise vortex pairs.

We then extend the analysis to general angular particles with different numbers of rotational symmetry folds n_{Ω}: RTF3 (three-fold tetrahedron), RCF3 (three-fold cube) and ROF4 (four-fold octahedron). We demonstrate that particle shape and rotation have a significant impact on wake stability, regime transitions and the resulting hydrodynamic forces. The vortex generation and suppression mechanisms observed for RCF4 are found to hold for other angular particles, with n_{Ω} emerging as a key factor in determining regime transitions. Additionally, the number of effective faces $N_{\mathcal{F}}$ alters the topology of the wake structures. In contrast, particle angularity ϕ plays a more dominant role in hydrodynamic forces, with higher angularity enhancing the Magnus effect especially in the low inertia flow. Using $N_{\mathcal{F}}$, we propose a generic model to predict the Strouhal number,

https://doi.org/10.1017/jfm.2025.10292 Published online by Cambridge University Press

which accurately captures the primary peaks of the frequency spectrum $\mathcal{S}tr_1$. We further show that increased n_Ω promotes vortex merging and suppression. Ultimately, this study demonstrates that wake flow stability can be effectively harnessed through the interplay between particle shape (ϕ, $N_\mathcal{F}$) and rotational properties (Ω, n_Ω).

This study presents a decoupled perspective on the complex interactions between a rotating particle and the surrounding fluid under controlled conditions. While freely moving particles introduce additional complexities– such as varying angular positions, added mass effects and particle–particle interactions– the findings from centre-fixed rotating particles provide valuable insights to comprehensively understand force balance and wake structure evolutions. These insights, in turn, aid in predicting the trajectories and regime transitions of freely settling angular particles. In addition, the deeper understanding we offer paves the way for advancements in controlling flow instabilities and optimising system designs across a variety of applications. Future research could explore a broader parameter space, particularly at $\Omega \geqslant 1$, to determine the threshold at which the influence of particle angularity becomes negligible and the effects of rotation dominate. This would provide a clearer understanding of when angularity can be disregarded in favour of rotational effects in flow stabilisation. Another intriguing direction would be to investigate streamwise rotating angular particles and compare their wake dynamics with those of the transversely rotating angular particles studied in this paper. Such a study could provide valuable perspectives into the most effective rotational strategies for stabilising the wake flow past angular particles.

Acknowledgement. Guodong Gai expresses his gratitude to the Pacific Institute of Mathematical Sciences for their support via his PIMS-CNRS postdoctoral fellowship.

Funding. The authors greatly appreciate the financial support of the Natural Sciences and Engineering Research Council of Canada (NSERC) via Anthony Wachs New Frontiers in Research Fund grant NFRFE-2018–01922. This research was enabled by support provided by Digital Research Alliance of Canada (https://alliancecan.ca/en) through Anthony Wachs' 2023–2024 Computing Resources for Research Groups allocation qpf-764-ac. This research was also supported in part through computational resources and services provided by Advanced Research Computing at the University of British Columbia (https://arc.ubc.ca).

Declaration of interests. The authors report no conflict of interest.

Appendix A. Distributed Lagrange multiplier/fictitious domain (DLM/FD) method

The governing equations for conservation of mass and momentum in an incompressible Newtonian fluid are given by

$$\rho_f^* \left(\frac{\partial \boldsymbol{u}^*}{\partial t^*} + \boldsymbol{u}^* \cdot \nabla \boldsymbol{u}^* \right) = -\nabla p^* + \mu_f^* \Delta \boldsymbol{u}^* \quad \text{in } \mathcal{D} \setminus P, \tag{A1}$$

$$\nabla \cdot \boldsymbol{u}^* = 0 \quad \text{in } \mathcal{D} \setminus P, \tag{A2}$$

where $\boldsymbol{u}^*$ denotes the fluid velocity vector, p^* represents the pressure, $\mathcal{D}$ is the computational domain and P refers to the solid particle.

The particle rotates around the z-axis with an imposed constant angular velocity, $\boldsymbol{\Omega}^*$, which remains unchanged throughout the simulations. The hydrodynamic force and torque (relative to the centre of mass) acting on the particle $\boldsymbol{F}^*$ and $\boldsymbol{T}^*$ are

$$\boldsymbol{F}^* = \int_{\partial P} \boldsymbol{\sigma}^* \cdot \hat{\boldsymbol{n}} \, \mathrm{d}S^*, \tag{A3}$$

$$\boldsymbol{T}^* = \int_{\partial P} \boldsymbol{r}^* \times \left(\boldsymbol{\sigma}^* \cdot \hat{\boldsymbol{n}} \right) \, \mathrm{d}S^*, \tag{A4}$$

https://doi.org/10.1017/jfm.2025.10292 Published online by Cambridge University Press

where $\hat{\boldsymbol{n}}$ is the outward-pointing unit normal vector to the particle surface ∂P, and the stress tensor for a Newtonian fluid is given by:

$$\boldsymbol{\sigma}^* = -p^* \boldsymbol{I_d} + 2\mu_f^* \boldsymbol{D}[\boldsymbol{u}]^*. \tag{A5}$$

The DLM/FD method combines the weak formulations of the fluid motion equation and the rigid particle motion equation to derive the governing equation for the fluid–particle mixture. First, the weak formulation for the fluid sub-domain $\mathcal{D} \setminus P$ is derived by enforcing rigid-body constraints on the particle surface ∂P. This formulation is then extended to the entire computational domain $\mathcal{D}$ by applying the rigid-body constraints across the entire particle domain P, leading to the combined equation of motion. The rigid-body motion constraints within the particle sub-domain are relaxed through the use of Lagrange multipliers, denoted as $\boldsymbol{\lambda}^*$. We define $\mathcal{W}_\Gamma$, $\mathcal{W}_0$, $\mathcal{L}_0$ and Λ as the functional spaces of the solution that satisfy the boundary conditions (Selçuk *et al.* 2021).

Next, we consider the following constrained optimisation problem for a single rotating particle P: find $\boldsymbol{u}^* \in \mathcal{W}_\Gamma$, $p^* \in \mathcal{L}_0^2$ and $\boldsymbol{\lambda}^* \in \Lambda$ such that we obtain the following.

(i) *Combined equations of motion:*

$$\int_{\mathcal{D}} \rho_f^* \left(\frac{\partial \boldsymbol{u}^*}{\partial t^*} + \boldsymbol{u}^* \cdot \nabla \boldsymbol{u}^* \right) \cdot \boldsymbol{v}^* \, \mathrm{d}\boldsymbol{x} - \int_{\mathcal{D}} p^* \nabla \cdot \boldsymbol{v}^* \mathrm{d}\boldsymbol{x} \tag{A6}$$

$$+ \int_{\mathcal{D}} \mu_f^* \nabla \boldsymbol{u}^* : \nabla \boldsymbol{v}^* \mathrm{d}\boldsymbol{x} = - \int_P \boldsymbol{\lambda}^* \cdot \boldsymbol{v}^* \, \mathrm{d}\boldsymbol{x}. \tag{A7}$$

(ii) *Continuity equation:*

$$\int_{\mathcal{D}} -q^* \nabla \cdot \boldsymbol{u}^* \, \mathrm{d}\boldsymbol{x} = 0. \tag{A8}$$

(iii) *For the particle:*

$$\left(1 - \frac{\rho_f^*}{\rho_p^*}\right) \frac{\mathrm{d}\boldsymbol{I}^* \boldsymbol{\Omega}^*}{\mathrm{d}t^*} \cdot \boldsymbol{\xi}^* = \int_P \boldsymbol{\lambda}^* \cdot \left(\boldsymbol{\xi}^* \times \boldsymbol{r}^* \right) \, \mathrm{d}\boldsymbol{x}, \tag{A9}$$

$$\int_P \boldsymbol{\alpha}^* \cdot \left(\boldsymbol{u}^* - (\boldsymbol{\Omega}^* \times \boldsymbol{r}^*) \right) \, \mathrm{d}\boldsymbol{x} = 0 \tag{A10}$$

for all $\boldsymbol{v}^* \in \mathcal{W}_0$, $\boldsymbol{\xi} \in \mathbb{R}^3$, $q^* \in \mathcal{L}^2(\mathcal{D})$ and $\boldsymbol{\alpha}^* \in \Lambda$. Equations (A6)–(A8) can be reformulated into a non-variational form, making them more suitable for spatial discretization using finite volume methods (Wachs *et al.* 2015; Selçuk *et al.* 2021).

We employ the DLM/FD solver developed and implemented by Selçuk *et al.* (2021) within Basilisk, an open-source code known for its ability to solve Navier–Stokes equations using adaptively refined octree Cartesian grids and the efficient convergence of its multigrid solvers for Poisson/Helmholtz-type problems (Popinet 2015). This method offers several advantages, including improved fluid–solid coupling through implicit hydrodynamic interaction calculations, and robust convergence properties of the Uzawa algorithm (Yu 2005; Wachs *et al.* 2015; Xia *et al.* 2022). For simulations involving rotating particles, we leverage our in-house Grains3D solver, which excels at handling rigid particles with complex shapes (Wachs *et al.* 2012; Rakotonirina *et al.* 2019). Further details on the implementation and validation of the DLM/FD solver can be found in our previous works (Wachs 2011; Wachs *et al.* 2015; Gai & Wachs 2023*b*, 2024).

https://doi.org/10.1017/jfm.2025.10292 Published online by Cambridge University Press

(*a*)

L_0	n_l	N_{cell}	$1/\Delta x$	$\overline{C_d}$
40	8	1.95×10^5	6	2.295
40	9	7.45×10^5	12	1.887
40	10	3.16×10^6	25	1.662
40	11	1.17×10^7	51	1.624
40	12	3.24×10^7	102	1.578

(*b*)

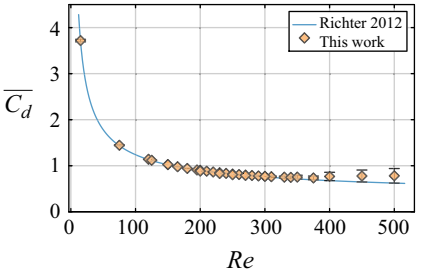

Figure 21. (*a*) Mesh convergence of $\overline{C_d}$ in the flow past a fixed tetrahedron at $Re = 100$ with grid refinement. L_0 denotes the dimensionless domain size, n_l the adaptive grid refinement level, N_{cell} the total number of cells and $1/\Delta x$ the number of cells per equivalent diameter. (*b*) Validation of $\overline{C_d}$ as a function of Re in the flow past a fixed cube with a face facing the flow, compared with Richter & Nikrityuk (2012).

Appendix B. Numerical validation: grid and time convergence

For the numerical validation of the DLM/FD solver, we investigate the impact of grid resolution on the convergence of the time-averaged drag coefficient, $\overline{C_d}$, for flow past a fixed tetrahedron and a fixed cube in figure 21. A domain size of $L_0 = 40$ was confirmed to be sufficiently large to eliminate boundary effects in our previous study (Gai & Wachs 2023*c*). Figure 21(*a*) illustrates the effect of mesh refinement, from $n_l = 8$ to $n_l = 12$, on $\overline{C_d}$ for flow at $Re = 100$ past a fixed tetrahedron, the most angular isometric polyhedron, with a triangular face facing the flow. The results show that $\overline{C_d}$ begins to converge at $1/\Delta x = 25$, with only a minor discrepancy of 2.83 % between $1/\Delta x = 51$ and $1/\Delta x = 102$. Beyond this level of refinement, higher grid resolution has a negligible impact on $\overline{C_d}$. Therefore, we confidently use a grid resolution of ($n_l = 12$, $1/\Delta x = 102$) for all computations in this study.

Furthermore, we perform a series of simulations of the flow past a fixed cube with a square face facing the flow, covering a Reynolds number range of $1 \leqslant Re \leqslant 500$. The results are presented in figure 21(*b*). For reference, we use the correlation provided by Richter & Nikrityuk (2012), which offers values of $\overline{C_d}$ for laminar flow past a fixed cube within the range $10 \leqslant Re \leqslant 250$. The grid resolution for these simulations is set to ($n_l = 12$, $1/\Delta x = 102$). Figure 21(*b*) shows excellent agreement between our numerical results with Richter's correlation (relative error $\varepsilon < 1\,\%$) for $10 \leqslant Re \leqslant 300$. For $300 \leqslant Re \leqslant 500$, higher relative errors ($1\,\% < \varepsilon < 10\,\%$) are observed. However, note that Richter's correlation is valid for $10 \leqslant Re \leqslant 250$ and has not been verified beyond this range. Additionally, the trend in $\overline{C_d}(Re)$ – featuring a plateau around $Re = 300{-}350$ followed by a slight increase – aligns well with numerical results from Seyed-Ahmadi & Wachs (2019) and Meng *et al.* (2021) under similar flow conditions. Therefore, the relative errors compared with Richter's correlation for $Re > 250$ are considered acceptable.

Accurate simulations of particle–flow interactions for a rotating angular particle requires careful choice of time resolution. In figure 22, we show the evolution of C_d and $C_{l,y}$ for a transversely rotating cube (RCF4) in the flow at $Re = 100$. Two scenarios must be considered separately: (i) for a slowly rotating particle, Δt needs to be large enough to capture a sufficient number of periods to accurately compute time-averaged physical quantities; (ii) for a rapidly rotating particle, a smaller Δt is necessary to ensure enough frames within a single period, thereby avoiding unphysical oscillatory signals.

In figures 22(*a*) and 22(*b*), we present the temporal evolution of C_d and $C_{l,y}$ for RCF4 at $\Omega = 0.1$. At this rotation rate, we observe that all four curves overlap as the time step

https://doi.org/10.1017/jfm.2025.10292 Published online by Cambridge University Press

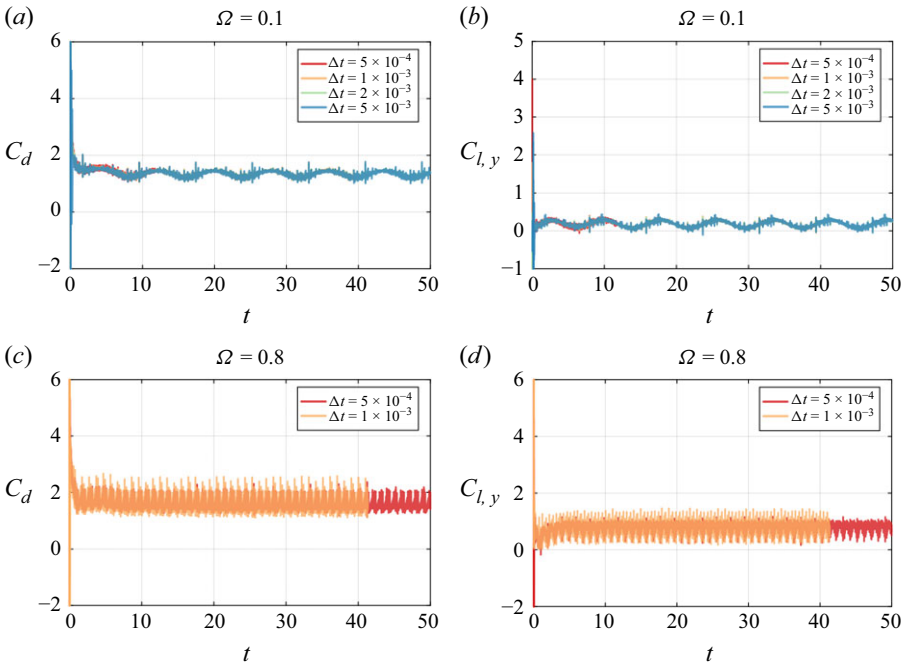

Figure 22. Temporal evolution of C_d and $C_{l,y}$ of the rotating RCF4 cube at: (*a*,*b*) $Re = 100$ and $\Omega = 0.1$, with increasing time step magnitude from $\Delta t = 5 \times 10^{-4}$ to 5×10^{-3}; (*c*,*d*) $Re = 100$ and $\Omega = 0.8$, from $\Delta t = 5 \times 10^{-4}$ to 1×10^{-3}.

increases from $\Delta t = 5 \times 10^{-4}$ to $\Delta t = 5 \times 10^{-3}$. A similar pattern is observed for lower rotation rates, $\Omega \leqslant 0.1$. Therefore, we select $\Delta t = 5 \times 10^{-3}$ as the maximum time step for these simulations. At higher rotation rates, such as $\Omega = 0.8$, we plot the temporal evolution of C_d and $C_{l,y}$ in figures 22(*c*) and 22(*d*). For these cases, a smaller time step is necessary, and we find that $\Delta t = 5 \times 10^{-4}$ closely matches the behaviour observed with $\Delta t = 1 \times 10^{-3}$ for both C_d and $C_{l,y}$. To achieve the best resolution in our simulations, we choose $\Delta t = 5 \times 10^{-4}$ as maximal time step for fast rotating cases, $\Omega > 0.1$. The time step selection in the simulations is adaptive and dynamic, carefully adjusted to satisfy the CFL condition. A more detailed and complete strategy for this approach is provided in (2.15).

Consequently, the chosen spatial and time resolutions for this study have been reliably validated, ensuring that the generated data set is free from significant biases due to computational spatial and temporal errors.

Appendix C. Vortex shedding and wake structures of RCF4

To provide a comprehensive view of regime transitions, figure 23 presents the vortical structures identified by $\lambda_2 = -1$ in the x-y plane for most cases of RCF4 investigated in this study, spanning $40 \leqslant Re \leqslant 400$ and $0.02 \leqslant \Omega \leqslant 1$. The vortical structures are coloured by u_x. The colour-coded boxes to the left of each case indicate the corresponding regimes, matching the regimes in figure 4. This vortex-shedding map illustrates the effects of varying Re and Ω on the wake instability. At low Ω and Re, the wake exhibits steady, straight or fragmented vortical structures. As both parameters increase, the flow becomes progressively more unsteady, with periodic vortex shedding patterns emerging in the HS regime. Vortex suppression is observed at $Re \leqslant 140$ and $\Omega \geqslant 0.3$ for RCF4. As Re and Ω

https://doi.org/10.1017/jfm.2025.10292 Published online by Cambridge University Press

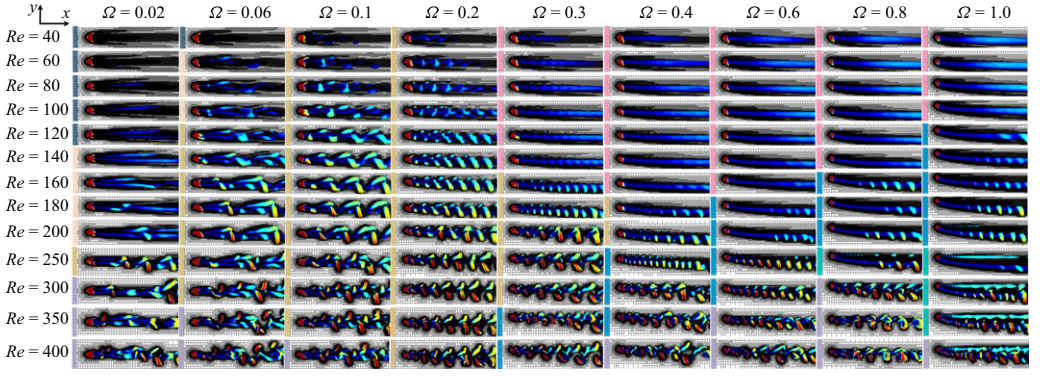

Figure 23. Vortex shedding and suppression in the wake of the rotating RCF4 cube in the x-y plane at $0.02 \leqslant \Omega \leqslant 1$ and $40 \leqslant Re \leqslant 400$. Isosurfaces are identified using the criterion $\lambda_2 = -1$, and coloured by streamwise velocity u_x, with red indicating high velocity and blue indicating low velocity.

further increase, the previously suppressed wake becomes unsteady again, transitioning to the HS, KH and DS regimes. At $Re \geqslant 400$, the flow generally transitions to a chaotic state, with the exception of the cases at $\Omega = 0.2$ and $\Omega = 0.3$.

Appendix D. Length and volume of recirculation region

In the study of flow past a fixed angular particle, the length, shape and size of the recirculation region play crucial roles in determining the pattern and frequency of vortex shedding, which significantly influence wake instability (Gai & Wachs 2023*b*). For rotating angular particles, this becomes even more pronounced, as the added rotational motion introduces complex interactions between the flow and the geometry of the particle, further impacting the structure and behaviour of the wake.

We define the recirculation region as the region where the streamwise velocity u_x is less than or equal to zero. Its volume is given by

$$V_r = \int_{\Omega} H(-u_x)\, dV = \sum_{i,j,k} \mathcal{H}(-u_x(i,\, j,\, k))\Delta V, \tag{D1}$$

where $u_x(i,\, j,\, k)$ is the streamwise velocity at the grid cell located at indices $(i,\, j,\, k)$. Here, $H(-u_x(i,\, j,\, k))$ is the discrete Heaviside function, which equals 1 if $u_x(i,\, j,\, k) \leqslant 0$, indicating flow reversal in that cell, and 0 otherwise. Additionally, $\Delta V = \Delta V^*/V^*_{sph}$ is the dimensionless volume of a single grid cell. Since the angular position of the rotating angular particles keeps changing in time, we define L_r as the x-component of the displacement from the particle centroid to the grid cell with the largest x-coordinate where the streamwise velocity component satisfies $u_x(i,\, j,\, k) \leqslant 0$. Mathematically, it can be expressed as

$$L_r = (\max\,(x_i \mid u_x(i,\, j,\, k) \leqslant 0) - x_p), \tag{D2}$$

where $x_p = x^*_p/D^*_{sph}$ is the dimensionless x-coordinate of the particle centroid.

We begin with RCF4 and then discuss the effects of particle angularity, as shown in figure 24. From figure 24(*a*), we observe that L_r of RCF4 increases with flow inertia for $40 \leqslant Re \leqslant 400$. At $Re \leqslant 200$, higher Ω results in a shorter L_r. For $Re \geqslant 250$, at $\Omega = 0.02$, the effects of rotation are minimal, with L_r values closely matching those of the fixed cube case in grey circles. However, as Ω increases, the trend becomes less obvious. Regarding

https://doi.org/10.1017/jfm.2025.10292 Published online by Cambridge University Press

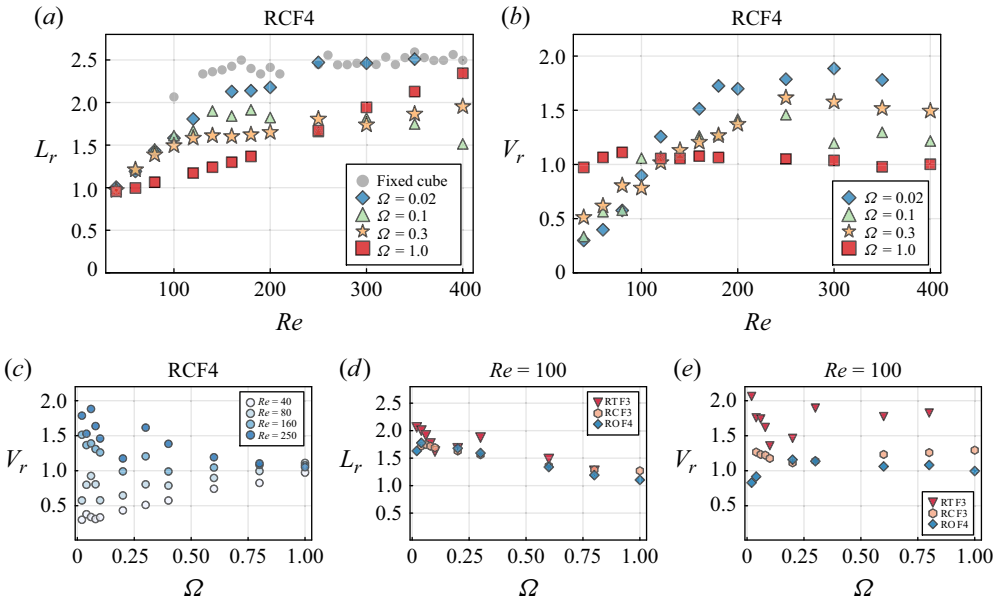

Figure 24. Evolution of recirculation region length L_r and volume V_r in the wake of a transversely rotating angular particle. RCF4: (*a*) L_r as a function of Re for increasing Ω, with reference values of the flow past a fixed cube plotted as grey dots; (*b*) V_r as a function of Re for different Ω; (*c*) V_r as a function of Ω for different Re. The effects of particle angularity on L_r and V_r as a function of Ω are depicted in panels (*d*) and (*e*), respectively.

the volume of the recirculation region, figure 24(*b*) shows that V_r increases with Re before reaching a plateau. For $Re \leqslant 100$, higher Ω results in a larger V_r. The slow-rotating cube at $\Omega = 0.02$ continues to exhibit an increase in V_r for $Re \geqslant 100$. Interestingly, for the fast-rotating cube at $\Omega = 1$, V_r remains approximately constant at $V_r \approx 1$ across the range $40 \leqslant Re \leqslant 400$. Additionally, for $Re \geqslant 250$, we observe that V_r at $\Omega = 0.3$ is larger than that at $\Omega = 0.1$, which can be attributed to the regime transition from the HS regime to the VS regime. This behaviour is further clarified in figure 24(*c*), where V_r is plotted as a function of Ω for several selected values of Re. It is important to note that even though the vortex within the recirculation region disappears in the VS regime, as observed in the rotating sphere case (Giacobello *et al.* 2009), the recirculation volume V_r, as defined in (D1), is not zero. Two key insights emerge from this figure: (i) V_r exhibits a local minimum at $\Omega = 0.2$, which corresponds to high-frequency vortex shedding, leading to a local maximum of the drag coefficient C_d, as shown in figure 12(*a*); (ii) as Ω increases, V_r converges to a value of approximately 1, regardless of the flow inertia. The rotational motion of the cube becomes dominant over the flow inertia, leading to a constant V_r. Yang *et al.* (2023) also observed that L_r becomes less sensitive to variations in Re for flow past a rotating short cylinder.

We further examine the effects of ϕ on L_r in figure 24(*d*), focusing on the RTF3, RCF3 and ROF4 cases. Since the three angular particles have the same volume, L_r exhibits a similar decreasing trend with increasing Ω. This occurs because, as Ω increases, the recirculation region shifts towards the lower part of the particle, reducing its extent in the streamwise direction. Similar results were reported for flow past a rotating short cylinder, where the decrease in L_r at high Ω was found to stabilise the flow (Yang *et al.* 2023). RTF3 shows slightly higher L_r values in the slow-rotating regimes (for example, $\Omega \leqslant 0.08$) than those of the other two particles. However, V_r increases clearly with the particle angularity,

https://doi.org/10.1017/jfm.2025.10292 Published online by Cambridge University Press

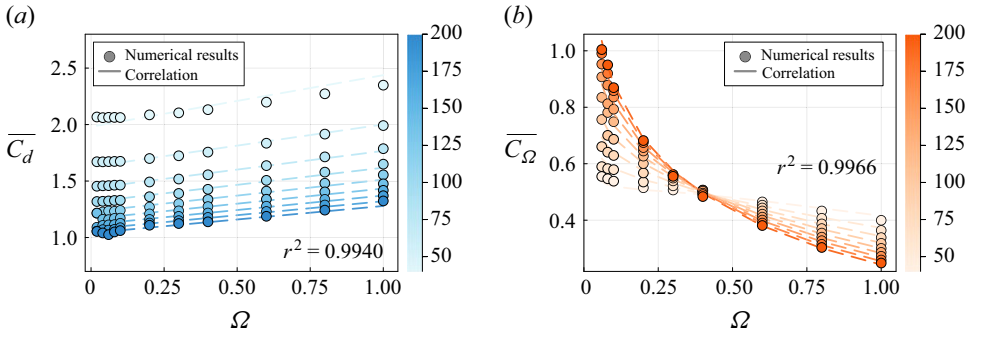

Figure 25. (*a*) Evolution of the time-averaged drag coefficient $\overline{C_d}$ of the rotating RCF4 cube as a function of Ω at $40 \leqslant Re \leqslant 200$ with increment $\Delta Re = 20$. (*b*) Evolution of $\overline{C_\Omega}$ at $40 \leqslant Re \leqslant 200$ with increment $\Delta Re = 20$ and $0.06 \leqslant \Omega \leqslant 1$. Our numerical simulation results (coloured circles) are compared with the empirical correlations from (E1) for C_d and (E2) for C_Ω, shown by dashed lines. Darker circles indicate higher values of Re.

i.e. as ϕ decreases. In figure 24(*e*), we note that RTF3 consistently exhibits larger V_r than those of RCF3 and ROF4 throughout the range $0.02 \leqslant \Omega \leqslant 1$. A local minimum in V_r around $\Omega \approx 0.2$ is observed for both RTF3 and RCF3.

Appendix E. Correlations for C_d and C_Ω at $Re \leqslant 200$

The drag coefficient plays a central role in fluid–particle interactions. However, existing correlations in the literature are typically derived for spheres or stationary particles, and thus fail to account for the added complexity introduced by angular particle rotation. For rotating cubes – like the RCF4 cube – the flow separation, wake structure and drag force differ significantly from spheres. Therefore, developing a new empirical correlation to the rotating cube is crucial for accurately modelling drag forces in CFD–DEM simulations.

Similarly to the $\overline{C_{l,y}}$ correlation, we derive an empirical correlation for $\overline{C_d}$ based on our numerical dataset within the range $40 \leqslant Re \leqslant 200$. To capture the influence of particle rotation, we introduce a correction factor to the classical drag correlation proposed by Schiller & Naumann (1935). Using multivariate regression, we determine the coefficients of each term and propose the following new correlation:

$$\overline{C_d} = \frac{24}{Re}(1 + 0.0628 Re^{0.833})(1.401 + 0.323\Omega), \tag{E1}$$

In this expression, the first term represents the Stokes drag, the second term accounts for inertial corrections and the third term captures the influence of cube rotation. A direct comparison with our numerical results is shown in figure 25(*a*) for varying Ω across the range of Reynolds number $40 \leqslant Re \leqslant 200$. The near-linear increase of $\overline{C_d}$ with Ω is accurately captured by the third term in (E1), while the decrease of $\overline{C_d}$ with increasing Re is also well represented. Overall, the proposed correlation in (E1) exhibits excellent agreement with the numerical results, achieving a coefficient of determination $R^2 = 0.9940$.

As discussed in § 4.4.3, the rotation coefficient C_Ω is of vital importance in force balance and trajectory instability analyses of freely moving particles. However, few studies have developed correlations for this important coefficient, especially in the context of rotating angular particles. To address this gap, we introduce a novel empirical correlation for $\overline{C_\Omega}$ as a function of Ω and Re, derived from our numerical dataset:

$$\overline{C_\Omega} = (0.0817 + 0.59\Omega)(4.75 + 0.17Re)\exp(-\Omega^{0.409} Re^{0.291}). \tag{E2}$$

https://doi.org/10.1017/jfm.2025.10292 Published online by Cambridge University Press

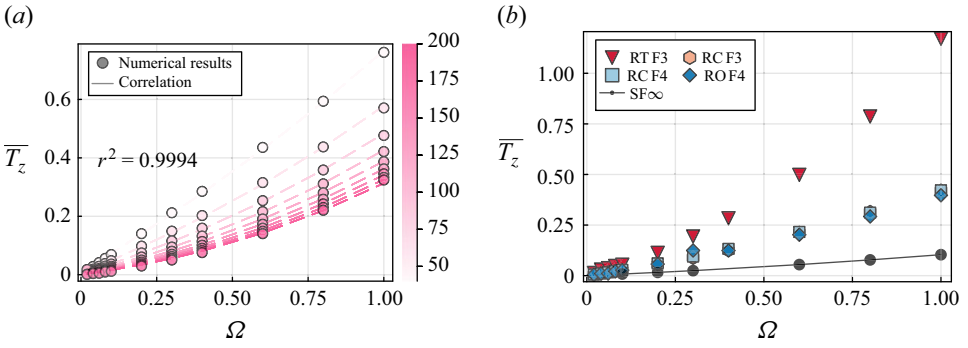

Figure 26. (*a*) Time-averaged torque $\overline{T_z}$ of the rotating RCF4 cube as a function of $0.02 \leqslant \Omega \leqslant 1$ at $40 \leqslant Re \leqslant 200$. The increasing darkness of the circles represents higher Re. For comparison, the empirical correlation in (F1) is illustrated by the dashed lines. (*b*) Effects of particle angularity on the $\overline{T_z}$ exerted on a rotating particle at $Re = 100$. The case of a rotating sphere ($RSF\infty$) at $Re = 100$ is provided as a reference and shown by the black solid line with circles.

This expression consists of two multiplicative factors accounting separately for the effects of flow inertia and particle rotation, followed by an exponential term that captures their coupling. Figure 25(*b*) compares the correlation and numerical results of $\overline{C_\Omega}$ for $40 \leqslant Re \leqslant 200$. The correlation accurately reflects the influences of both Re and Ω, achieving an overall coefficient of determination $R^2 = 0.9966$. In addition, the invariance region of $\overline{C_\Omega}$ with respect to Re at $\Omega = 0.3{-}0.4$ is well captured by the balance between the linear term $4.75 + 0.17\,Re$ and the exponential term $\exp\left(-\Omega^{0.409}\,Re^{0.291}\right)$ in (E2).

Appendix F. Hydrodynamic torque on the rotating angular particle

In addition to drag and lift forces, hydrodynamic torques are instrumental in determining the trajectories of freely moving particles. They alter particle angular positions, rotation velocities and thereby affect the Magnus effect, which is particularly significant for non-spherical particles (Fernandes *et al.* 2008; Ern et al. 2009; Gai & Wachs 2024).

We thoroughly examine and present the evolution of the time-averaged torque, $\overline{T_z}$, using (2.6) for a rotating RCF4 cube at $40 \leqslant Re \leqslant 200$, as shown in figure 26(*a*). Since Ω is imposed and held constant, $\overline{T_z}$ reflects the hydrodynamic response of the fluid to the rotating particle. Clearly, $\overline{T_z}$ increases with Ω. At higher Re, flow inertia dominates over viscous forces, resulting in a thinner boundary layer and reduced shear stresses that generate torque. Moreover, the decrease of $\overline{T_z}$ is less pronounced with increasing flow inertia to $200 \leqslant Re \leqslant 400$ (data not shown for brevity). To better understand the coupling between Re and Ω and their overall effect on $\overline{T_z}$, we establish a simple scaling relation for $\overline{T_z}$ as follows:

$$\overline{T_z} = 0.2\Omega^2 \left(1 + 4.743\Omega^{-1.1}\frac{24}{Re}\right). \tag{F1}$$

This relation matches the numerical results for $40 \leqslant Re \leqslant 200$ remarkably well, with $R^2 = 0.9994$ as indicated in figure 26(*a*). It is interesting to note that for small Re and Ω, $\overline{T_z}$ scales with the Stokes drag factor $24/Re$. In particular, as Re approaches zero, $\overline{T_z}$ varies linearly with Ω, a behaviour that is consistent with the observations in figure 26(*a*).

How does $\overline{T_z}$ evolve for particles of different shapes? In figure 26(*b*), we compute and present $\overline{T_z}$ for particles with varying angularities and rotational symmetry folds $N_{\mathcal{F}}$

https://doi.org/10.1017/jfm.2025.10292 Published online by Cambridge University Press

at $Re = 100$. We observe that RTF3, which has high angularity ($\phi = 0.67$), exhibits a higher value of $\overline{T_z}$ than cubes ($\phi = 0.806$) and octahedrons ($\phi = 0.846$). The difference between RTF3 and the other angular particles becomes more pronounced with increasing Ω, reaching up to 2.8 times that of RCF4 at $\Omega = 1$. From figure 26(*b*), the difference between cubes and octahedrons are quite subtle. As a reference, $\overline{T_z}$ of a rotating sphere is also provided, and it is smaller than that of all angular particles. Overall, the particle angularity is a key factor playing a more significant role than the rotational symmetry fold $N_{\mathcal{F}}$ on the evolution of $\overline{T_z}$.

Similar trends are also observed at $Re = 60$ and 160 (data not shown for brevity). Note that for these particles, the other two components of the hydrodynamic torque, $\overline{T_x}$ and $\overline{T_y}$, are much smaller than $\overline{T_z}$ at $60 \leqslant Re \leqslant 160$ and are therefore not discussed. An exception is observed for RTF3, where the tetrahedron high angularity results in a non-negligible $\overline{T_x}$, unlike the cases for the cube, octahedron or sphere. A comprehensive investigation of hydrodynamic torque components requires a wider range of particle shapes and axis of rotation to draw more general conclusions.

References

Angle, B.R., Rau, M.J. & Byron, M.L. 2024 Settling of nonuniform cylinders at intermediate Reynolds numbers. *Phys. Rev. Fluids* **9** (7), 070501.

Baker, L.J. & Coletti, F. 2021 Particle–fluid–wall interaction of inertial spherical particles in a turbulent boundary layer. *J. Fluid Mech.* **908**, A39.

Best, J.L. 1998 The influence of particle rotation on wake stability at particle Reynolds numbers, $Re_P <$ 300—implications for turbulence modulation in two-phase flows. *Intl J. Multiphase Flow* **24** (5), 693–720.

Bonnefis, P., Sierra-Ausin, J., Fabre, D. & Magnaudet, J. 2024 Path instability of deformable bubbles rising in Newtonian liquids: a linear study. *J. Fluid Mech.* **980**, A19.

Chaparian, E. & Frigaard, I.A. 2021 Clouds of bubbles in a viscoplastic fluid. *J. Fluid Mech.* **927**, R3.

Chen, W., Rheem, C.-K., Lin, Y. & Li, Y. 2020 Experimental investigation of the whirl and generated forces of rotating cylinders in still water and in flow. *Intl J. Nav. Archit. Ocean Engng* **12**, 531–540.

Citro, V., Tchoufag, J., Fabre, D., Giannetti, F. & Luchini, P. 2016 Linear stability and weakly nonlinear analysis of the flow past rotating spheres. *J. Fluid Mech.* **807**, 62–86.

Clanet, C. 2015 Sports ballistics. *Annu. Rev. Fluid Mech.* **47** (2015), 455–478.

Daghooghi, M. & Borazjani, I. 2018 The effects of irregular shape on the particle stress of dilute suspensions. *J. Fluid Mech.* **839**, 663–692.

De, A.K. & Sarkar, S. 2023 Wake instability behind a streamwise and transversely rotating sphere. *Phys. Rev. Fluids* **8** (2), 024101.

Dupuy, D., Ansart, R. & Simonin, O. 2024 Investigation of near-wall particle statistics in CFD-DEM simulations of dense fluidised beds and derivation of an Eulerian particle dynamic wall boundary condition. *J. Fluid Mech.* **982**, A2.

Ern, P., Risso, F., Fernandes, P.C. & Magnaudet, J. 2009 Dynamical model for the buoyancy-driven zigzag motion of oblate bodies. *Phys. Rev. Lett.* **102** (13), 134505.

Fernandes, P.C., Ern, P., Risso, F. & Magnaudet, J. 2008 Dynamics of axisymmetric bodies rising along a zigzag path. *J. Fluid Mech.* **606**, 209–224.

Gai, G. & Wachs, A. 2023*a* Dynamics, wakes, and regime transitions of a fixed angular particle in an unbounded inertial flow. I. Regular tetrahedron angular position. *Phys. Rev. Fluids* **8**, 064304.

Gai, G. & Wachs, A. 2023*b* Dynamics, wakes, and regime transitions of a fixed angular particle in an unbounded inertial flow. II. From tetrahedron to sphere. *Phys. Rev. Fluids* **8**, 064305.

Gai, G. & Wachs, A. 2023*c* High fidelity adaptive Cartesian octree grid computations of the flow past a Platonic polyhedron up to a Reynolds number of 200. *Powder Technol.* **420**, 118390.

Gai, G. & Wachs, A. 2023*d* On the streamwise vorticity generation and distribution in an angular particle wake. *J. Fluid Mech.* **964**, R3.

Gai, G. & Wachs, A. 2024 On the dynamics and wakes of a freely settling Platonic polyhedron in a quiescent Newtonian fluid. *J. Fluid Mech.* **985**, A3.

Giacobello, M., Ooi, A. & Balachandar, S. 2009 Wake structure of a transversely rotating sphere at moderate Reynolds numbers. *J. Fluid Mech.* **621**, 103–130.

https://doi.org/10.1017/jfm.2025.10292 Published online by Cambridge University Press

GLOWINSKI, R., PAN, T.W., HESLA, T.I. & JOSEPH, D.D. 1999 A distributed Lagrange multiplier/fictitious domain method for particulate flows. *Intl J. Multiphase Flow* **25** (5), 755–794.

GOYAL, A., GAI, G., CHENG, Z., CUNHA, J.P., ZHU, L. & WACHS, A. 2024 Flow past a random array of statistically homogeneously distributed stationary Platonic polyhedrons: data analysis, probability maps and deep learning models. *Intl J. Multiphase Flow* **177**, 104854.

HARDY, B., FEDE, P. & SIMONIN, O. 2024 Theoretical derivation and a priori validation of a new scalar variance-based sub-grid drag force model for simulation of gas–solid fluidized beds. *Powder Technol.* **436**, 119454.

JEONG, J. & HUSSAIN, F. 1995 On the identification of a vortex. *J. Fluid Mech.* **285**, 69–94.

JIMÉNEZ-GONZÁLEZ, J.I., MANGLANO-VILLAMARÍN, C. & COENEN, W. 2019 The role of geometry on the global instability of wakes behind streamwise rotating axisymmetric bodies. *Eur. J. Mech. B - Fluids* **76**, 205–222.

KANG, S., CHOI, H. & LEE, S. 1999 Laminar flow past a rotating circular cylinder. *Phys. Fluids.* **11** (11), 3312–3321.

KARIMI-ZINDASHTI, G. & KURÇ, Ö 2024 Flow past rotating cylinders using deterministic vortex method. *Ocean Engng* **291**, 116342.

KHAN, M.A., ANWER, S.F., KHAN, S.A. & HASAN, N. 2021 Vortex shedding suppression of vibrating square cylinder in mixed convection regime. *Phys. Fluids.* **33** (12), 123610.

KIM, J., CHOI, H., PARK, H. & YOO, J.Y. 2014 Inverse magnus effect on a rotating sphere: when and why. *J. Fluid Mech.* **754**, R2.

KLOTZ, L., GOUJON-DURAND, S., ROKICKI, J. & WESFREID, J.E. 2014 Experimental investigation of flow behind a cube for moderate Reynolds numbers. *J. Fluid Mech.* **750**, 73–98.

MARQUARDT, J.E., HAFEN, N. & KRAUSE, M.J. 2024 A novel model for direct numerical simulation of suspension dynamics with arbitrarily shaped convex particles. *Comput. Phys. Commun.* **304**, 109321.

MENG, Q., AN, H., CHENG, L. & KIMIAEI, M. 2021 Wake transitions behind a cube at low and moderate Reynolds numbers. *J. Fluid Mech.* **919**, A44.

MERCIER, M.J., WANG, S., PÉMÉJA, J., ERN, P. & ARDEKANI, A.M. 2020 Settling disks in a linearly stratified fluid. *J. Fluid Mech.* **885**, A2.

NIAZMAND, H. & RENKSIZBULUT, M. 2003 Surface effects on transient three-dimensional flows around rotating spheres at moderate Reynolds numbers. *Comput. Fluids.* **32** (10), 1405–1433.

OESTERLÉ, B. & DINH, T.BUI 1998 Experiments on the lift of a spinning sphere in a range of intermediate Reynolds numbers. *Exp. Fluids.* **25** (1), 16–22.

POON, E.K.W., OOI, A.S.H., GIACOBELLO, M. & COHEN, R.C.Z. 2013 Hydrodynamic forces on a rotating sphere. *Intl J. Heat Fluid Flow* **42**, 278–288.

POON, E.K.W., OOI, A.S.H., GIACOBELLO, M., IACCARINO, G. & CHUNG, D. 2014 Flow past a transversely rotating sphere at Reynolds numbers above the laminar regime. *J. Fluid Mech.* **759**, 751–781.

POPINET, S. 2015 A quadtree-adaptive multigrid solver for the Serre–Green–Naghdi equations. *J. Comput. Phys.* **302**, 336–358.

RAHMANI, M., BANAEI, A.A., BRANDT, L. & MARTINEZ, D.M. 2023 Stochastic model for predicting the shape of flexible fibers in suspensions. *Phys. Rev. Fluids* **8** (2), 024306.

RAHMANI, M., GUPTA, A. & JOFRE, L. 2022 Aggregation of microplastic and biogenic particles in upper-ocean turbulence. *Intl J. Multiphase Flow* **157**, 104253.

RAHMANI, M. & WACHS, A. 2014 Free falling and rising of spherical and angular particles. *Phys. Fluids.* **26** (8), 083301.

RAKOTONIRINA, A.D., DELENNE, J.-Y., RADJAI, F. & WACHS, A. 2019 Grains3D, a flexible DEM approach for particles of arbitrary convex shape—Part III: extension to non-convex particles modelled as glued convex particles. *Comput. Part. Mech.* **6** (1), 55–84.

RASHIDI, S., HAYATDAVOODI, M. & ESFAHANI, J.A. 2016 Vortex shedding suppression and wake control: a review. *Ocean Engng* **126**, 57–80.

RICHTER, A. & NIKRITYUK, P.A. 2012 Drag forces and heat transfer coefficients for spherical, cuboidal and ellipsoidal particles in cross flow at sub-critical reynolds numbers. *Intl J. Heat Mass Transfer* **55** (4), 1343–1354.

RUBINOW, S.I. & KELLER, J.B. 1961 The transverse force on a spinning sphere moving in a viscous fluid. *J. Fluid Mech.* **11** (3), 447–459.

SAHA, A.K. 2004 Three-dimensional numerical simulations of the transition of flow past a cube. *Phys. Fluids.* **16** (5), 1630–1646.

SAREEN, A., HOURIGAN, K. & THOMPSON, M.C. 2024 Varying Magnus effect on a rotating sphere at intermediate Reynolds numbers. *Intl J. Heat Fluid Flow* **109**, 109501.

SCHILLER, L. & NAUMANN, A. 1935 A drag coefficient correlation. *Zeitschrift des Vereins Deutscher Ingenieure* **77**, 318–320.

https://doi.org/10.1017/jfm.2025.10292 Published online by Cambridge University Press

SELÇUK, C., GHIGO, A.R., POPINET, S. & WACHS, A. 2021 A fictitious domain method with distributed Lagrange multipliers on adaptive quad/octrees for the direct numerical simulation of particle-laden flows. *J. Comput. Phys.* **430**, 109954.

SEYED-AHMADI, A. & WACHS, A. 2019 Dynamics and wakes of freely settling and rising cubes. *Phys. Rev. Fluids* **4** (7), 074304.

SEYED-AHMADI, A. & WACHS, A. 2020 Microstructure-informed probability-driven point-particle model for hydrodynamic forces and torques in particle-laden flows. *J. Fluid Mech.* **900**, A21–1–38.

SEYED-AHMADI, A. & WACHS, A. 2021 Sedimentation of inertial monodisperse suspensions of cubes and spheres. *Phys. Rev. Fluids* **6** (4), 044306.

SHI, P. & RZEHAK, R. 2019 Lift forces on solid spherical particles in unbounded flows. *Chem. Engng Sci.* **208**, 115145.

SIERRA-AUSÍN, J., LORITE-DÍEZ, M., JIMÉNEZ-GONZÁLEZ, J.I., CITRO, V. & FABRE, D. 2022 Unveiling the competitive role of global modes in the pattern formation of rotating sphere flows. *J. Fluid Mech.* **942**, A54.

TANG, H., *et al.* 2024 Injectable ultrasonic sensor for wireless monitoring of intracranial signals. *Nature* **630** (8015), 84–90.

TOROBIN, L.B. & GAUVIN, W.H. 1959 Fundamental aspects of solids-gas flow: Part I: Introductory concepts and idealised sphere motion in viscous regime. *Can. J. Chem. Engng* **37** (4), 129–141.

TSUJI, Y., MORIKAWA, Y. & MIZUNO, O. 1985 Experimental measurement of the Magnus force on a rotating sphere at low Reynolds numbers. *J. Fluids Engng* **107** (4), 484–488.

WACHS, A. 2009 A DEM-DLM/FD method for direct numerical simulation of particulate flows: sedimentation of polygonal isometric particles in a Newtonian fluid with collisions. *Comput. Fluids.* **38** (8), 1608–1628.

WACHS, A. 2011 PeliGRIFF, a parallel DEM-DLM/FD direct numerical simulation tool for 3D particulate flows. *J. Engng Maths* **71** (1), 131–155.

WACHS, A., GIROLAMI, L., VINAY, G. & FERRER, G. 2012 Grains3D, a flexible DEM approach for particles of arbitrary convex shape — Part I: Numerical model and validations. *Powder Technol.* **224**, 374–389.

WACHS, A., HAMMOUTI, A., VINAY, G. & RAHMANI, M. 2015 Accuracy of finite volume/staggered grid distributed Lagrange multiplier/fictitious domain simulations of particulate flows. *Comput. Fluids.* **115**, 154–172.

WANG, Z., XIAO, Y., LIU, J., SUN, H., LIU, J., LIANG, D., ZHANG, T. & ZHANG, PEI 2024 Investigation on settling behavior of single cuboid-like particle in a quiescent fluid. *Powder Technol.* **439**, 119713.

XIA, Y., YU, Z., PAN, D., LIN, Z. & GUO, Y. 2022 Drag model from interface-resolved simulations of particle sedimentation in a periodic domain and vertical turbulent channel flows. *J. Fluid Mech.* **944**, A25.

YANG, Y., WANG, C., GUO, R. & ZHANG, M. 2023 Numerical analyses of the flow past a short rotating cylinder. *J. Fluid Mech.* **975**, A15.

YU, Z. 2005 A DLM/FD method for fluid/flexible-body interactions. *J. Comput. Phys.* **207** (1), 1–27.

https://doi.org/10.1017/jfm.2025.10292 Published online by Cambridge University Press